

## Cadmium(II) and Nickel(II) Complexes of Benziporphyrins. A Study of Weak Intramolecular Metal–Arene Interactions

Marcin Stępień, Lechosław Latos-Grazyński,\* Ludmiła Szterenberga, Jarosław Panek, and Zdzisław Latajka

Contribution from the Department of Chemistry, University of Wrocław, 14 F. Joliot-Curie St., Wrocław 50 383, Poland

Received November 3, 2003; E-mail: llg@wchuwr.chem.uni.wroc.pl

**Abstract:** Weak metal–arene interactions have been investigated in Zn, Cd, Hg, and Ni complexes of *meso*-tetraaryl *m*- and *p*-benziporphyrin (**1** and **2**) and of the new compound, *m*-benziporphodimethene (**3**). Compounds **1–3** incorporate the phenylene moiety into a macrocyclic structure so as to facilitate the interaction between the arene and coordinated metal ion. X-ray studies performed on Cd(II) and Ni(II) complexes show that the arene fragment approaches the ion at a distance much shorter than the sum of van der Waals radii. In chloronickel(II) *m*-benziporphyrin, a weak agostic bond is actually formed. In the NMR spectra of the Cd(II) and Hg(II) species, unusual  $^1\text{H}$ –M and  $^{13}\text{C}$ –M scalar couplings have been observed that are transmitted directly between the metal and the arene. DFT calculations performed for two Cd(II) species and subsequent AIM analysis show that the accumulation of electron density between the metal and arene necessary to induce these couplings is fairly small and the interaction is steric in nature. In the paramagnetic Ni(II) complexes of **1** and **3**, the agostic proton of the *m*-phenylene exhibits large downfield  $^1\text{H}$  NMR shifts (386 and 208 ppm at 298 K, respectively). An agostic mechanism of spin density transfer is proposed to explain these shifts as resulting from electron donation from the CH bond to the metal. In chloronickel(II) *p*-benziporphyrin, the inner protons of the *p*-phenylene have a contrastingly small shift (0.0 ppm at 298 K), indicating that in this case the agostic interaction is inefficient, in agreement with the X-ray data.

### Introduction

The existence of a chemical bond is commonly assessed on the basis of the interatomic distance. The optimum bond length depends on the identity of atoms involved, their chemical environment, and the amount of available electron density. On the other hand, nonbonding distances are most conveniently defined by intramolecular contacts, from which van der Waals radii are usually calculated.<sup>1</sup> Such a definition of chemical bond relies on the fact that interatomic distances falling between the “bonding” and “nonbonding” limits are seldom observed. Those cases, however, are very interesting from the theoretical point of view.

The interactions between arene rings and metal ions, observed in solution and in the solid state, provide examples of particular geometrical flexibility (Figure 1). A CH moiety of the arene may participate in  $\eta^n$  bonding ( $\pi$ -arene complex, Figure 1A) but can also form a  $\sigma$ -bond or an agostic bond with the metal (Figure 1B and C, respectively). On the other end of the scale lies the van der Waals interaction (Figure 1D), wherein no sharing of electron density occurs between the metal and arene.

Unusual cases of metal–arene bonding are encountered in various areas of inorganic chemistry. Coordination geometries intermediate between  $\pi$ - and  $\sigma$ -bonding were observed in the arene complexes of the silylium ion,  $\text{R}_3\text{Si}^+$ ,<sup>2–4</sup> and triarylalu-

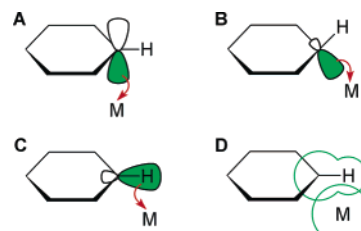


Figure 1. Limiting types of metal–arene interaction.

minum,  $(\text{C}_6\text{F}_5)_3\text{Al}$ .<sup>5</sup> The existence of so-called “longer-range”  $\eta^6$  interactions with the arene was proved by statistical analysis for main group metals, and for  $d^{10}$  transition metal ions, such as Ag(I) and Hg(II).<sup>6</sup> Those interactions are characterized by the  $\text{M}\cdots\text{Ct}$  distance of 2.5–3.5 Å (Ct is the ring centroid), which is normally less than the sum of the metal van der Waals radius and half-thickness of the benzene ring.

The strength of the interaction can be varied by appropriate modifications of the coordinating environment of the metal. For instance, it was possible to stabilize unusual arene–iron(III) porphyrin pairs in the solid state by introducing a virtually

(1) Bondi, A. J. *J. Phys. Chem.* **1964**, *68*, 441.

(2) Lambert, J. B.; Zhang, S.; Stern, C.; Huffman, J. *Science* **1993**, *260*, 1917.  
 (3) Reed, C. A.; Xie, Z.; Bau, R.; Benesi, A. *Science* **1993**, *262*, 402.  
 (4) Reed, C. A. *Acc. Chem. Res.* **1998**, *31*, 325.  
 (5) Hair, G. S.; Cowley, A. H.; Jones, R. A.; McBurnett, B. G.; Voigt, A. J. *Am. Chem. Soc.* **1999**, *121*, 4922.  
 (6) Mascal, M.; Kerdellhué, J.-L.; Blake, A. J.; Cooke, P. A.; Mortimer, R. J.; Teat, S. J. *Eur. J. Inorg. Chem.* **2000**, 485.

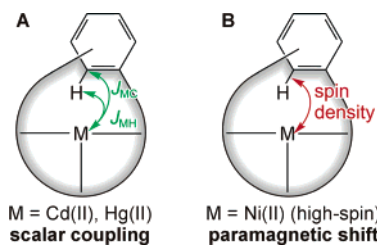


**Figure 2.** NMR spectroscopic probes used for investigating the metal–arene interaction in benziporphyrin complexes.

noncoordinating counterion (carborane).<sup>7,8</sup> In Hg(II) complexes, use of weak ligands such as trifluoroacetate,<sup>9</sup>  $\text{AlCl}_4^-$ , or  $\text{GaCl}_4^-$  leads to significant strengthening of  $\text{Hg}\cdots\text{arene}$  interactions.<sup>9–11</sup>

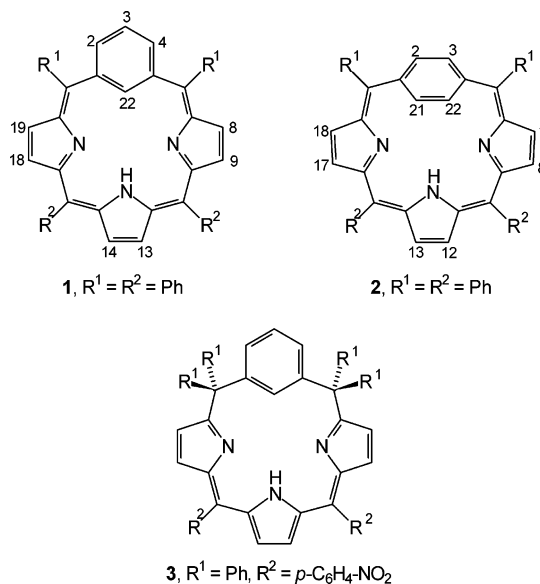
The weaker interactions are often insufficient to stabilize the M–arene complex, which is held together by additional intramolecular restraints, such as those imposed by a pincer ligand<sup>12,13</sup> or a cage structure.<sup>6,14,15</sup> Such restraints can also be introduced by incorporating the arene moiety into an appropriately sized macrocycle, as shown schematically in Figure 2. The macrocyclic brace binds the metal ion and holds it close to the arene fragment.

Benziporphyrins, a recently developed class of macrocycles,<sup>16–19</sup> realize the above concept of ligand construction by fusing the structural motifs of porphyrin and benzene (Scheme 1). These new molecules belong to the family of carbaporphyrins, porphyrin analogues with a C–H bond in the coordination core.<sup>20,21</sup> Tetraaryl-*meta*-benziporphyrin (**1**) and its *para* isomer<sup>19</sup> (**2**) have already been shown to coordinate metal ions. In the case of a *p*-benziporphyrin cadmium(II) complex, a weak M–arene interaction could be observed both in the solid state and in solution.<sup>19</sup> Unusual arene coordination modes were also investigated in palladium(II) oxybenziporphyrins.<sup>22</sup>

The goal of the present work is to investigate metal–arene interactions in complexes of benziporphyrins **1,2** and the new compound, hexaaryl-*m*-benziporphodimethene (**3**), and to show how this weak bonding affects NMR spectroscopic parameters.

The first part of our study deals with the diamagnetic Zn(II), Cd(II), and Hg(II) species. The experimental approach exploits our previous finding<sup>19</sup> that the proximity of the metal ion and arene gives rise to observable  $^1\text{H}$ –X and  $^{13}\text{C}$ –X scalar couplings in the NMR spectra (Figure 2A). Such couplings are

**Scheme 1**



usually classified as “through-space” or “nonbonding”, because their magnitude cannot be rationalized in terms of the network of formal bonds in the molecule.<sup>23</sup> Here, couplings with the spin-active nuclei of  $^{111}\text{Cd}$ ,  $^{113}\text{Cd}$ , and  $^{199}\text{Hg}$  ( $I = 1/2$ ) are used to detect the unusual metal–arene interaction.<sup>24</sup>

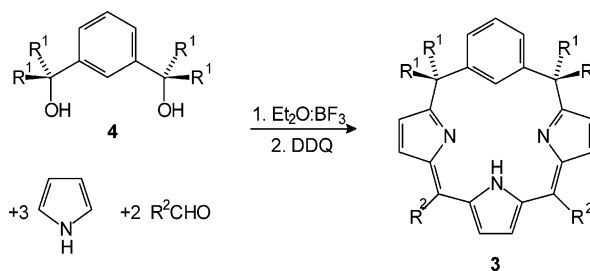
In a complementary investigation, the metal–arene interaction in high-spin Ni(II) benziporphyrins has been probed using their paramagnetically shifted  $^1\text{H}$  NMR spectra. The paramagnetic metal center induces unusual chemical shifts of the proximate protons. These shifts are largely due to direct spin delocalization onto the arene ring and may be considered an effect of the metal–arene interaction (Figure 2B).

To complement the NMR and X-ray studies, the electronic structure of selected systems has been analyzed by DFT modeling and subsequent AIM analysis.

## Results and Discussion

**Synthesis.** 6,11,16,21-Tetraphenyl-*m*-benziporphyrin (**1**) and 5,10,15,20-tetraphenyl-*p*-benziporphyrin (**2**) were synthesized as described previously.<sup>18,19</sup> The synthesis of 6,6,21,21-tetraphenyl-11,16-bis(4-nitrophenyl)-*meta*-benziporphodimethene (**3**) builds on the same methodology of mixed condensation, as shown in Scheme 2 (yield 14%).

**Scheme 2**

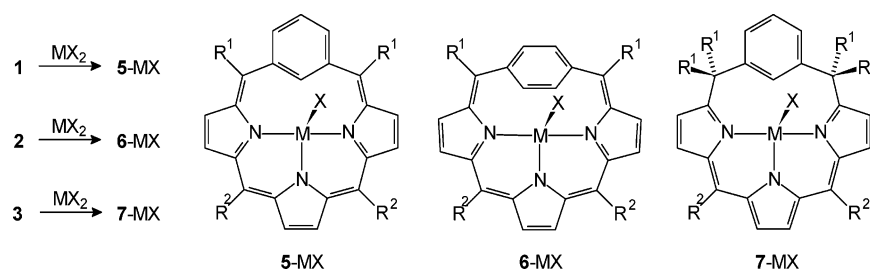


Insertion of zinc(II), cadmium(II), mercury(II), and nickel(II) into **1–3** has been readily achieved by boiling a mixture of the free base and an appropriate salt, usually anhydrous chloride,

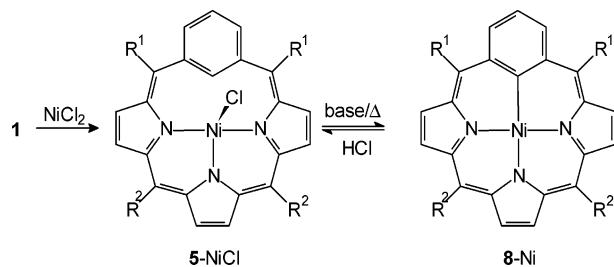
- (7) Xie, Z.; Bau, R.; Reed, C. A. *Angew. Chem., Int. Ed. Engl.* **1994**, *33*, 2433.
- (8) Evans, D. R.; Fackler, N. L. P.; Xie, Z.; Rickard, C. E. F.; Boyd, P. D. W.; Reed, C. A. *J. Am. Chem. Soc.* **1999**, *121*, 8466.
- (9) Lau, W.; Huffman, J. C.; Kochi, J. K. *J. Am. Chem. Soc.* **1982**, *104*, 5515.
- (10) Borovik, S. A.; Bott, S. G.; Barron, A. R. *Angew. Chem., Int. Ed.* **2000**, *39*, 4117.
- (11) Borovik, S. A.; Bott, S. G.; Barron, A. R. *J. Am. Chem. Soc.* **2001**, *123*, 11219.
- (12) Vignalok, A.; Uzan, O.; Shimon, L. J. W.; Ben-David, Y.; Martin, J. M. L.; Milstein, D. *J. Am. Chem. Soc.* **1998**, *120*, 12539.
- (13) Dani, P.; Karlen, T.; Gossage, R. A.; Smeets, W. J. J.; Spek, A. L.; van Koten, G. *J. Am. Chem. Soc.* **1997**, *119*, 11317.
- (14) Fages, F.; Desvergne, J.-P.; Bouas-Laurent, H.; Marsau, P.; Lehn, J. M.; Kotzyba-Hibert, F.; Albrecht-Gary, A. M.; Al-Joubbeh, M. *J. Am. Chem. Soc.* **1989**, *111*, 8672.
- (15) Howarth, O. W.; Nelson, J.; McKee, V. *Chem. Commun.* **2000**, 21.
- (16) Berlin, K.; Breitmaier, E. *Angew. Chem., Int. Ed. Engl.* **1994**, *33*, 1246.
- (17) Lash, T. D. *Angew. Chem., Int. Ed. Engl.* **1995**, *34*, 2533.
- (18) Stepień, M.; Latos-Grażyński, L. *Chem.-Eur. J.* **2001**, *7*, 5113.
- (19) Stepień, M.; Latos-Grażyński, L. *J. Am. Chem. Soc.* **2002**, *124*, 3838.
- (20) Latos-Grażyński, L. Core Modified Heteroanalogues of Porphyrins and Metalloporphyrins. In *The Porphyrin Handbook*; Kadish, K. M., Smith, K. M., Guilard, R., Eds.; Academic Press: New York, 2000; Vol. 2, Chapter 14, pp 361–416.
- (21) Furuta, H.; Maeda, H.; Osuka, A. *Chem. Commun.* **2002**, 1795.
- (22) Stepień, M.; Latos-Grażyński, L.; Lash, T. D.; Sztterenber, L. *Inorg. Chem.* **2001**, *40*, 6892.

- (23) Hilton, J.; Sutcliffe, L. H. *Prog. Nucl. Magn. Reson. Spectrosc.* **1975**, *10*, 27.
- (24) Contreras, R. H.; Facelli, J. C. *Annu. Rep. NMR Spectrosc.* **1993**, *27*, 255.

## Scheme 3



## Scheme 4



in a chloroform or chloroform/acetonitrile solution (Scheme 3). In most cases, yields are quantitative (see Experimental Section). The resulting complexes will be denoted **5–MX** (*m*-benzporphyrin), **6–MX** (*p*-benzporphyrin), and **7–MX** (*m*-benzporphodimethene).

When **5–NiCl** is refluxed in the reaction mixture, it gradually transforms into **8–Ni**, a diamagnetic, square-planar complex with a  $\sigma$ -aryl bond (Scheme 4). **8–Ni** is an analogue of the palladium(II) and platinum(II) species reported earlier for *m*-benzporphyrin,<sup>18</sup> and its formation is facilitated by the presence of base (anhydrous  $\text{K}_2\text{CO}_3$ ). The M–C bond in **8–Ni** is cleaved by addition of gaseous HCl to a  $\text{CHCl}_3$  solution, leading back to the desired paramagnetic complex **5–NiCl**. Actually, the latter reaction has been used preparatively to obtain **5–NiCl**.

**X-ray Crystallographic Studies.** X-ray analyses have been performed for compounds **5–CdCl**, **5–NiCl**, and **6–NiCl**. The pertinent crystal structure of **6–CdCl** was reported in our previous communication.<sup>19</sup> Crystal data are given in Table S1 (Supporting Information).

The *m*-benzporphyrin cadmium complex, **5–CdCl**, crystallizes in space group  $P\bar{1}$ , with two independent molecules in the asymmetric unit. The two molecules, A and B, have nearly identical geometry (Figure 3, Table 1). The Cd–N and Cd–Cl bond lengths are directly comparable to those reported for **6–CdCl**,<sup>19</sup> with the Cd–N(24) bond systematically shorter than the other two Cd–N distances. The Cd ion in **5–CdCl** is displaced from the  $\text{N}_3$  plane by ca. 0.9 Å toward the chloride, which is significantly more than in **6–CdCl**. As a consequence, the value of the N(23)–Cd–N(25) angle decreases from 153° in **6–CdCl** to 132° in **5–CdCl**.

The *m*-phenylene unit of **5–CdCl** approaches the cadmium ion more closely than does the *p*-phenylene of **6–CdCl**. While the  $\text{Cd}\cdots\text{C}$  separation is only slightly reduced (2.71 Å in **5–CdCl** versus 2.76 Å in **6–CdCl**), the  $\text{Cd}\cdots\text{H}$  distances are markedly shorter (ca. 2.67 Å in **5–CdCl** and 3.07 Å in **6–CdCl**). The  $\text{Cd}\cdots\text{C}(22)$  distance in **5–CdCl** exceeds the typical Cd–C

bond lengths (2.10–2.35 Å)<sup>25</sup> but is much smaller than the corresponding van der Waals contact (3.3 Å).<sup>1</sup> The mutual orientation of the Cd ion and *m*-phenylene is shown in the inset of Figure 3.

Coordination of the metal ion does not significantly influence the C–C bond lengths in the macrocycle, which are similar to those reported for the free base 22-acetoxybenzporphyrin.<sup>18</sup> Again, the tripyrrolic fragment shows localization of double bonds corresponding to the valence structure **1** (Scheme 1), while the *m*-phenylene ring retains a virtually unperturbed benzene geometry.

The crystal structure of the *m*-benzporphyrin nickel(II) complex, **5–NiCl**, is visualized in Figure 4. The smaller ionic radius of high-spin Ni(II) is responsible for the majority of structural differences between **5–NiCl** and **5–CdCl** (Table 1). In particular, the Ni(II) ion lies only 0.46 Å above the  $\text{N}_3$  plane.

The  $\text{Ni}\cdots\text{C}(22)$  and  $\text{Ni}\cdots\text{H}(22)$  distances are 2.549(3) and 2.40(3) Å. These values are very small as compared to the van der Waals contact<sup>1</sup> (3.4 Å for  $\text{Ni}\cdots\text{C}$ ) and evidence the formation of a weak agostic bond. In addition, careful analysis of available crystal data (Table S2, Supporting Information) confirms that the C–H bond is not coplanar with the phenylene ring (Figure 4, inset), which is also indicative of an agostic interaction. The distance between the H(22) atom and the C(1)C(22)C(5) plane is 0.14(3) Å, which corresponds to an angle of 8.4(1.8)° between the C(22)–H(22) bond and the bisector of the C(1)–C(22)–C(5) angle. The C(22)–H(22) bond length is 0.96(3) Å; that is, no elongation is observed within the experimental error.

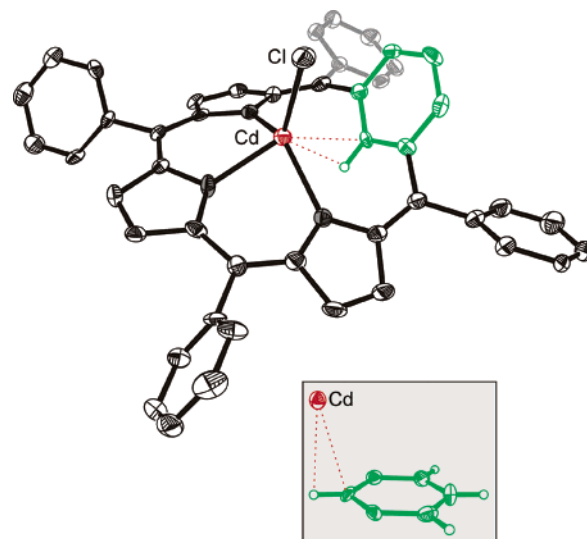


**Figure 3.** Crystal structure of **5–CdCl**. Thermal ellipsoids are at the 50% probability level. Hydrogen atoms and solvent molecules are omitted for clarity. Inset shows the geometry of the  $\text{Cd}\cdots\text{arene}$  interaction.

(25) Hursthouse, M. B.; Motevalli, M.; O'Brien, P.; Walsh, J. R.; Jones, A. C. *Organometallics* **1991**, *10*, 3196.

**Table 1.** Selected Structural Data for Complexes **5**–CdCl, **6**–CdCl, **5**–NiCl, and **6**–NiCl

	5–CdCl		6–CdCl <sup>a</sup>	5–NiCl	6–NiCl
	molecule A	molecule B			
	Distance/Å				
M–Cl	2.417(2)	2.431(2)	2.435(1)	2.281(1)	2.240(1)
M–N(23/25)	2.281(4), 2.287(4)	2.261(4), 2.268(4)	2.289(1), 2.290(1)	2.042(3), 2.033(3)	2.163(3), 2.170(3)
M–N(24)	2.209(4)	2.201(5)	2.201(1)	1.950(3)	1.977(3)
M···C(22)	2.722(5)	2.709(5)		2.549(3)	
M···C(21/22)			2.748(2), 2.762(2)		2.583(4), 2.587(4)
M···H(22)	2.74(5)	2.59(5)		2.40(3)	
M···H(21/22)			3.06(2), 3.08(2)		2.80, 2.81
M···N <sub>3</sub>	0.94	0.91	0.52	0.46	0.17
	Angle/deg				
Cl–M–N(24)	125.0(1)	127.4(1)	129.0(1)	104.5(1)	119.3(1)
N(23)–M–N(25)	131.0(2)	132.2(2)	153.3(1)	152.5(1)	170.6(1)
Cl–M–C(22)	101.8(1)	98.2(1)		94.0(1)	
Cl–M–C(21/22)			108.5(1), 106.9(1)		100.5(1), 100.2(1)
C <sub>6</sub> /N <sub>3</sub>	51.7	52.0	44.5	56.8	42.0
N <sub>3</sub> /6,21–Ph	24.7, 26.5	26.3, 29.6		20.3, 18.5	
N <sub>3</sub> /5,20–Ph			50.4, 43.4		40.9, 50.1
N <sub>3</sub> /11,16–Ph	52.1, 56.2	51.3, 58.4		57.6, 53.7	
N <sub>3</sub> /10,15–Ph			66.2, 63.9		58.5, 63.6

<sup>a</sup> Data for **6**–CdCl correspond to the structure published in ref 18.

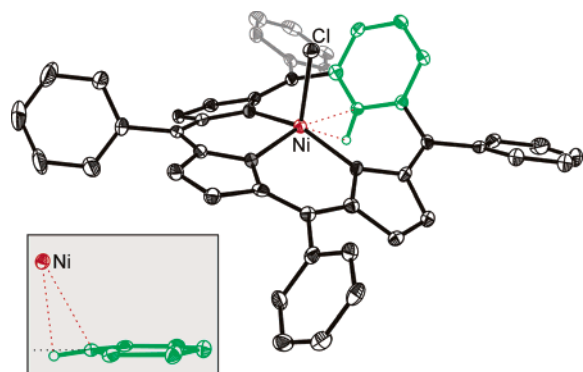


**Figure 4.** Crystal structure of **5**–NiCl. Thermal ellipsoids are at the 50% probability level. Hydrogen atoms and solvent molecules are omitted for clarity. Inset shows the geometry of the Ni···arene interaction (black dotted line indicates the bisector of the C(1)C(22)C(5) angle).

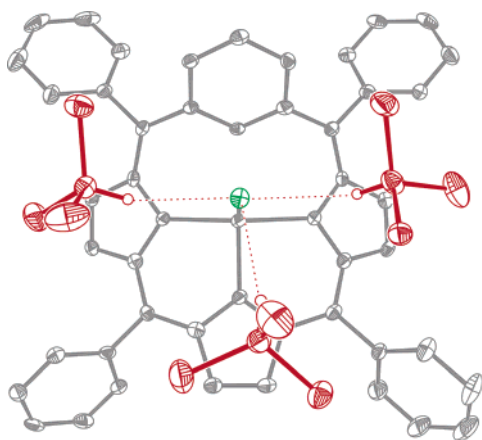


**Figure 5.** Hydrogen-bonding pattern between three CHCl<sub>3</sub> molecules (red) and the axial chloride (green) of **5**–NiCl (crystal structure).

In the crystal lattice, the axial chloride of **5**–NiCl is surrounded by three molecules of chloroform, which form weak hydrogen bonds, with CH···Cl distances in the range 2.52–2.72 Å (Figure 5).

Figure 6 shows the crystal structure of chloronickel(II) *p*-benzporphyrin (**6**–NiCl). The projection has been chosen so as to emphasize boatlike puckering of the *p*-phenylene, which

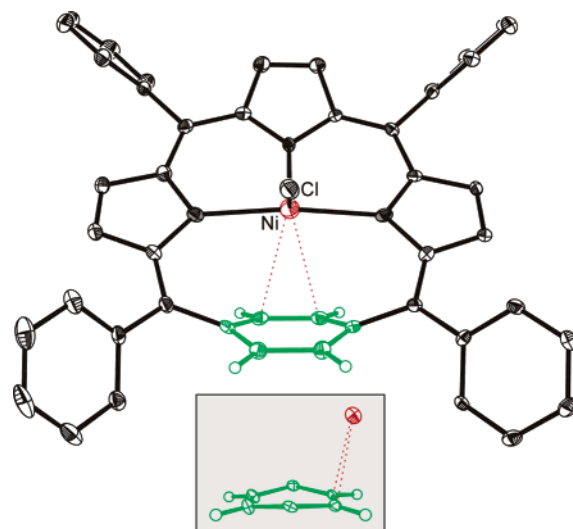


**Figure 6.** Crystal structure of **6**–NiCl. Thermal ellipsoids are at the 50% probability level. Hydrogen atoms and solvent molecules are omitted for clarity. Inset shows the geometry of the Ni···arene interaction.

is caused by the macrocyclic restraint. This puckering can be quantified as the average deviation of the C(1) and C(4) atoms from the mean plane of atoms C(2)C(3)C(21)C(22). The deviation equals 0.16 Å for **6**–NiCl and **6**–CdCl, slightly more than in the reported structures of the free base **2** and its diacid (0.10–0.12 Å).<sup>19</sup>

The molecular geometry of **6**–NiCl is similar to that of the cadmium counterpart, **6**–CdCl. However, the small Ni(II) ion better fits the coordination core, which results in a closer approach of the metal to the *p*-phenylene fragment. The Ni···C(21/22) distances of 2.58 and 2.59 Å are nearly as short as the Ni···C(22) separation in **5**–NiCl (2.55 Å). However, different positioning of the Ni ion with respect to the phenylene results in a 0.4 Å increase of the Ni···H distances. As we shall see later, this geometrical difference has a profound effect on the NMR spectra of **5**–NiCl and **6**–NiCl.

It should be noted that the Ni···arene interaction found in **5**–NiCl and **6**–NiCl is fairly untypical. Paramagnetic organonickel compounds are extremely rare,<sup>20</sup> the few examples

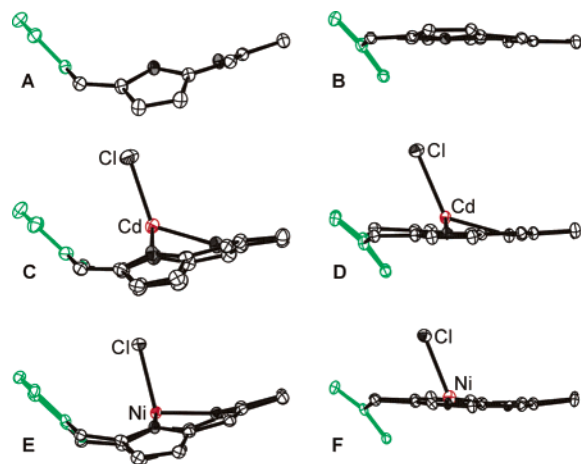


**Figure 7.** Side views of free base 22-acetoxyporphyrin<sup>18</sup> (A) and *p*-benzporphyrin<sup>19</sup> (B), and complexes 5–CdCl (C), 6–CdCl<sup>19</sup> (D), 5–NiCl (E), and 6–NiCl (F). Hydrogen atoms, meso substituents, and the 22-AcO group (in structure A) have been omitted for clarity.

including species with a  $\sigma$ -bound methyl group (Ni–C distance of 2.04(1) Å)<sup>26</sup> or a  $\eta^5$ -cyclopentadienyl group (mean distance of 2.27 Å),<sup>27</sup> and the idonickel(II) complex of 2,21-dimethylated N-confused porphyrin (2.404(9) Å).<sup>28</sup>

The Ni–N(23/25) bonds are noticeably longer in 6–NiCl (2.17 Å) than in 5–NiCl (2.04 Å) and are the longest Ni–N distances ever seen for high-spin nickel(II) porphyrins<sup>29</sup> and core-modified porphyrins.<sup>20</sup> The N(23)⋯N(25) separation in free base acetoxybenzporphyrin<sup>18</sup> and *p*-benzporphyrin<sup>19</sup> is 4.19 and 4.59 Å, respectively (see Table S3, Supporting Information for additional parameters). The latter value is fairly large, especially when compared to the trans N⋯N distance in tetraphenylporphyrin (4.11 Å, tetragonal form).<sup>30</sup> Thus, the macrocycle of *p*-benzporphyrin is unable to compress sufficiently upon coordination of the Ni(II) ion, which results in the observed elongation of Ni⋯N(23/25) bonds.

It is instructive to compare the side views of free base benzporphyrins and the four Ni and Cd complexes (Figure 7). Interestingly, the degree of tilt adopted by the phenylene moiety in *m*- and *p*-benzporphyrin is not affected by coordination. (It can be argued that the conformation of 22-acetoxyporphyrin,<sup>18</sup> shown in Figure 7A, is induced by the bulk of the 22-OAc substituent, but a preliminary structure of the 22-unsubstituted **1** has shown an identical degree of nonplanarity.) The observed similarity of conformations between complexes and free ligands does not implicate rigidity of the macrocycles. The ligands are in fact flexible; **1** forms planar complexes, such as **8**–Ni, while **2** was reported to undergo dynamic processes in solution.<sup>19</sup>

When complexes of **1** and **2** with the same metal are compared, the *p*-benzporphyrin species is always characterized by a smaller distance between the ion and the N<sub>3</sub> plane and, presumably as a consequence, by a smaller Cl–M–N(24) angle

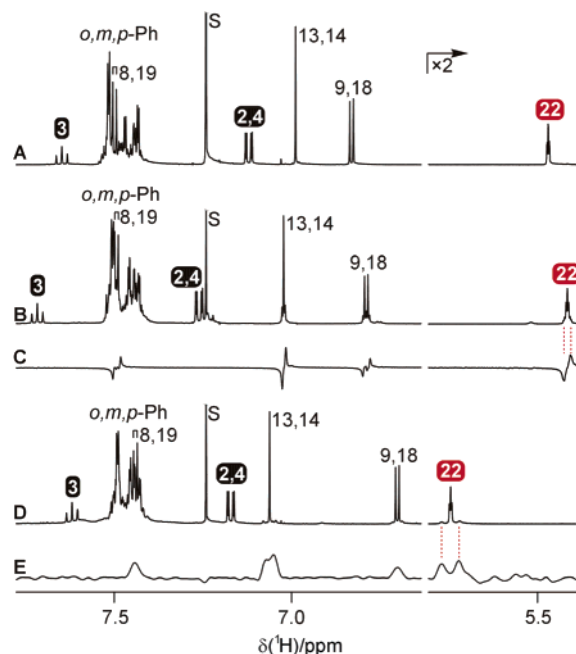


**Figure 8.** <sup>1</sup>H NMR spectra (CDCl<sub>3</sub>, 298 K) of complexes 5–ZnCl, 5–CdCl, and 5–HgCl (traces A, B, and D, respectively). Trace C shows a 1D gsHSQC spectrum of 5–CdCl ( $\tau_f = 20$  ms) showing the pattern of <sup>13</sup>Cd satellites (in antiphase). Trace E shows a 1D gsHMQC spectrum of 5–HgCl ( $\tau_f = 20$  ms, magnitude mode).

(Table 1). These regularities probably arise from the difference in shape between the coordination cores of *m*- and *p*-benzporphyrin.

#### NMR Spectra of Diamagnetic Benzporphyrin Complexes.

Zn(II), Cd(II), and Hg(II) complexes of benzporphyrins **1**–**3** yield well-resolved NMR spectra, which have been used to study the metal–arene interaction. The proximity of the phenylene fragment to the metal ion induces direct scalar couplings between the spin-active nucleus of the metal (<sup>111/113</sup>Cd, <sup>199</sup>Hg) and the nearby <sup>1</sup>H or <sup>13</sup>C nuclei.

Figure 8 shows the <sup>1</sup>H NMR spectra of *m*-benzporphyrin complexes 5–ZnCl, 5–CdCl, and 5–HgCl (traces A, B, and D, respectively). The three complexes share a common spectral pattern, which is in accord with the solid-state molecular structure determined for 5–CdCl. In particular, the marked differentiation of 8,19-H and 9,18-H chemical shifts (ca. 0.7 ppm) is caused by the orientation of meso substituents. Due to significant ruffling of the macrocycle on the side of the *m*-phenylene, the 6,21-Ph rings are nearly coplanar with the macrocycle, which results in deshielding of the 8,19 protons. Analogous differentiation of shifts was recently reported for chlorozinc(II) acetoxybenzporphyrin.<sup>31</sup>

<sup>1</sup>H NMR spectra of 6–ZnCl, 6–CdCl, 7–ZnCl, and 7–CdCl and selected UV–vis spectra are given in the Supporting Information (Figures S3–S6).

Interaction with the spin-active Cd and Hg nuclei leads to scalar couplings observed in the <sup>1</sup>H NMR spectra. These couplings generate characteristic satellite patterns, which can be extracted from the 1D spectrum using appropriate filtering techniques (Figure 8, traces C and E).  $\beta$ -Pyrrolic protons exhibit the usual four-bond couplings, also known for regular Cd and Hg porphyrins.<sup>32</sup> “Through-bond” couplings are also observed

- (26) Ram, M. S.; Riordan, C. G.; Yap, G. P. A.; Liables-Sands, L.; Rheingold, A. L.; Marchaj, A.; Norton, J. R. *J. Am. Chem. Soc.* **1997**, *119*, 1648.  
 (27) Kläui, W.; Huhn, M.; Herbst-Irmer, R. *J. Organomet. Chem.* **1991**, *415*, 133.  
 (28) Chmielewski, P. J.; Latos-Grażyński, L.; Głowiak, T. *J. Am. Chem. Soc.* **1996**, *118*, 5690.  
 (29) Kirner, J. F.; Garaofolo, J., Jr.; Scheidt, W. R. *Inorg. Nucl. Chem. Lett.* **1975**, *11*, 107.  
 (30) Hamor, M. J.; Hamor, T. A.; Hoard, J. L. *J. Am. Chem. Soc.* **1964**, *86*, 1938.

- (31) Stępień, M.; Latos-Grażyński, L. *Inorg. Chem.* **2003**, *42*, 6183.

**Table 2.** Selected Spectral Parameters Derived from  $^1\text{H}$  and  $^{13}\text{C}$  NMR Spectra for the Free Bases **1–3** and Their Complexes **5–7** ( $\text{CDCl}_3$ , 298 K)<sup>a</sup>

compound	$\delta_{\text{H}}$ /ppm	$\delta_{\text{C}}$ /ppm	$^1J_{\text{CH}}$ /Hz	$J_{\text{HH}}$ /Hz	$K_{\text{MH}}$ / $10^{19} \text{ T}^2 \text{ J}^{-1}$	$J_{\text{HC}}$ /Hz	$K_{\text{MC}}$ / $10^{19} \text{ T}^2 \text{ J}^{-1}$
<i>meta</i> -Benzporphyrin and Its Complexes							
<b>1</b> (free base) <sup>b</sup>	7.33	109.4	167.3				
<b>5–ZnCl</b>	5.51	85.8	158.6				
<b>5–CdCl</b>	5.46	82.8	159.4	7.5	2.8	13.6	20.1
<b>5–HgCl</b>	5.80	89.2	162.3	23.7	10.9	26 <sup>d</sup>	47 <sup>d</sup>
<b>5–HgO<sub>2</sub>CCF<sub>3</sub></b>	5.63	85.6	n.m.	38.2	17.6	46 <sup>d</sup>	84 <sup>d</sup>
<i>para</i> -Benzporphyrin and Its Complexes							
<b>2</b> (free base) <sup>c</sup>	5.24 <sup>e</sup>	130.1 <sup>e</sup>	n.m.				
<b>6–ZnCl</b>	1.33	133.1	n.m.				
		(131.1 <sup>f</sup> )					
<b>6–CdCl</b> <sup>c</sup>	1.69	134.6	167	4.4	1.6	≤6.5	≤9.6
		(130.1 <sup>f</sup> )	(167 <sup>f</sup> )				
<i>m</i> -Benzporphodimethene and Its Complexes							
<b>3</b> (free base)	7.68	136.1	n.m.				
<b>7–ZnCl</b>	7.34	128.1	n.m.				
<b>7–CdCl</b>	7.23	126.5	n.m.	9.5	3.5	~9	~13

<sup>a</sup> The data correspond to position 22 (*m*-benzporphyrin, *m*-benzporphodimethene, and their complexes, **1**, **3**, **5–MX**, **7–MX**) or to positions 21,22 (*p*-benzporphyrin and its complexes, **2** and **6–MX**).  $J$  constants (absolute values) are determined with an estimated error of ca. 0.3 Hz ( $J_{\text{CdH}}$ ) and at least 1 Hz ( $J_{\text{CdC}}$ ). Reduced coupling constants are defined as  $K_{\text{AX}} = 4\pi^2 J_{\text{AX}} / h\gamma_{\text{A}}\gamma_{\text{X}}$ . n.m. = not measured. <sup>b</sup> Reference 18. <sup>c</sup> Reference 19. <sup>d</sup> Coupling constant  $J_{\text{HgC}}$  extracted from a high-resolution HSQC spectrum (see Supporting Information, estimated error  $\pm 5$  Hz). <sup>e</sup> Mean value for the 2,3,21,22 signal in the fast exchange limit;<sup>19</sup> at 168 K, signal 21,22-H lies at 2.32 ppm. <sup>f</sup> Value for 2,3-H.

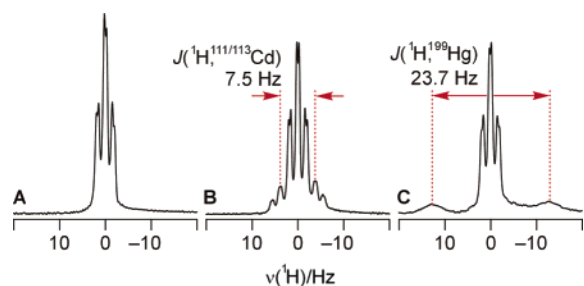


**Figure 9.** Multiplet patterns of the 22-H signal in the  $^1\text{H}$  NMR spectra of **5–ZnCl** (A,  $\delta = 5.51$  ppm), **5–CdCl** (B,  $\delta = 5.45$  ppm), and **5–HgCl** (C,  $\delta = 5.79$  ppm). In all cases, the homonuclear couplings are  $^4J_{2,4-22} = 1.7$  Hz and  $^5J_{3-22} = 0.3$  Hz.

for pyrrolic and meso carbons in  $^{13}\text{C}$  NMR (Table S4, Supporting Information).

More importantly, satellite patterns are also seen for 22-H (in **5–MX** and **7–MX**) and 21,22-H (in **6–MX**). These couplings are too large to be of the usual “through-bond” origin because the metal nucleus and the proton are in all cases six bonds apart and the geometry of the bond path is unfavorable. These couplings are therefore a result of the weak metal–arene interaction. The relevant data for cadmium and mercury species are collected in Table 2. Figure 9 shows the 22-H multiplet patterns displayed by **5–ZnCl**, **5–CdCl**, and **5–HgCl**. In the case of the zinc species (trace A), only a triplet of doublets is observed, which corresponds to homonuclear  $^4J_{\text{HH}}$  and  $^5J_{\text{HH}}$  couplings (with 2,4-H and 3-H, respectively). In the Cd species, **5–CdCl** (trace B), the central line, which corresponds to the molecules containing spin-inactive Cd isotopes, is flanked with a pair of satellites reproducing the homonuclear splitting pattern. The coupling constant  $J_{\text{CdH}}$  is 7.5 Hz. The mercury complex,

**5–HgCl** (trace C), exhibits a significantly larger coupling (23.7 Hz), but the satellites are broadened due to exchange (**5–HgCl** has been observed to equilibrate rapidly with traces of free base **1**) or specific relaxation mechanisms (e.g., chemical shift anisotropy).<sup>33</sup> The actual  $J_{\text{HgH}}$  value may therefore be slightly larger than that quoted here.

The magnitude of couplings depends on the structure of the macrocycle. In the cadmium series, **6–CdCl** displays a  $J_{\text{CdH}}$  coupling of 4.4 Hz,<sup>19</sup> whereas in the *m*-benzporphodimethene species, **7–CdCl**,  $J_{\text{CdH}}$  is 9.5 Hz; that is, it exceeds the constant measured for its *m*-benzporphyrin congener. In addition, the couplings are strongly affected by the axial ligand. Replacing the chloride of **5–HgCl** with trifluoroacetate results in a remarkable increase of  $J_{\text{HgH}}$  from 23.7 to 38.2 Hz.

It is also possible to determine the corresponding  $J_{\text{CdC}}$  and  $J_{\text{HgC}}$  coupling constants (Table 2). Interestingly, they follow trends similar to those of the respective metal–proton couplings.

Direct comparison of the Cd and Hg  $J$  couplings requires their conversion to the reduced values  $K$ , which are independent of the gyromagnetic ratios of the coupled nuclei (Table 2). The reduced constants found for Hg species are in all cases larger than the respective values calculated for Cd counterparts. Apparently, the more diffuse nature of the Hg ion results in a more efficient overlap of electron density between the metal and arene. In addition, the  $K_{\text{MC}}$  constants given in Table 2 are always larger than the corresponding  $K_{\text{MH}}$  values.

**Agostic Interaction in Diamagnetic Benzporphyrin Complexes.** Scalar couplings between two nuclei of a molecule that are proximate in the spatial sense (internuclear distance) but not in the topological sense (number of intervening chemical bonds) are called “through-space” or “nonbonding”.<sup>23,24,34</sup> The latter name suggests absence of any direct bonding, which may not always be the case, while the former term incorrectly implies that electron density is not involved in this type of coupling. Conversely, all scalar couplings, whether transmitted by covalent bonds, hydrogen bonds,<sup>35</sup> or nonbonding interactions (e.g., in van der Waals molecules),<sup>36,37</sup> have a common physical origin. Here, we denote the “nonbonding” couplings simply as  $J_{\text{XY}}$ , with no indication of the bond path (as in  $^1J$ ,  $^2J$ , etc.).

Indeed, in most cases such unusual couplings were considered to result from steric congestion rather than from sharing of electron density. The mechanism of  $\text{F}\cdots\text{F}$  nonbonding scalar couplings proposed by Mallory<sup>38</sup> involves a pair of doubly occupied nonbonding orbitals, whose interaction offers no energetic advantage but facilitates communication between nuclear spins. An interesting example of nonbonding coupling that involved a metallic element was provided by a dithallium cryptate,<sup>15</sup> in which a  $J(^1\text{H}-^{203/205}\text{Tl})$  value of 17 Hz was found (the corresponding X-ray  $\text{Tl}\cdots\text{H}$  distance was 3.82 Å). However, the  $\text{CH}\cdots\text{Pt(II)}$  interactions investigated by Pregosin et al.,<sup>39–43</sup> which led to  $J_{\text{PtH}}$  couplings of 8–39 Hz, and  $J_{\text{PtC}}$  couplings of comparable magnitude, were termed “weak agostic bonds”. Those bonds differed from “conventional” agostic interactions

(32) Jakobsen, H. J.; Ellis, P. D.; Inners, R. R.; Jensen, C. F. *J. Am. Chem. Soc.* **1982**, *104*, 7742.

(33) Ghosh, P.; Desrosiers, P. J.; Parkin, G. *J. Am. Chem. Soc.* **1998**, *120*, 10416.  
 (34) Mallory, F. B.; Mallory, C. W.; Butler, K. E.; Lewis, M. B.; Xia, A. Q.; Luzik, E. D., Jr.; Fredenburgh, L. E.; Ramanjulu, M. M.; Van, Q. N.; Francl, M. M.; Freed, D. A.; Wray, C. C.; Hann, C.; Nerz-Stormes, M.; Carroll, P. J.; Chirlian, L. E. *J. Am. Chem. Soc.* **2000**, *122*, 4108.  
 (35) Gemmecker, G. *Angew. Chem., Int. Ed.* **2000**, *39*, 1224.  
 (36) Bagno, A.; Saielli, G.; Scorrano, G. *Angew. Chem., Int. Ed.* **2001**, *40*, 2532.  
 (37) Bagno, A.; Saielli, G.; Scorrano, G. *Chem.-Eur. J.* **2002**, *8*, 2047.  
 (38) Mallory, F. B. *J. Am. Chem. Soc.* **1973**, *95*, 7747.

in several respects; in particular, the  $^1\text{H}$  chemical shifts experienced a downfield, rather than upfield, relocation with respect to the nonagostic reference.<sup>44</sup> Moreover, the  $^1J_{\text{CH}}$  coupling constant of the agostic CH moiety only showed a slight decrease relative to the reference system. The observed Pt $\cdots$ H distances were in the range of 2.3–2.9 Å.

The present case of cadmium benziporphyrins also shows that for weak interactions the parameters  $\delta_{\text{H}}$ ,  $^1J_{\text{CH}}$ , and  $J_{\text{MH}}$  are not necessarily correlated. While the 22-H signals of complexes **5**–MX experience remarkable upfield shifts relative to free base **1** (up to 1.9 ppm), the effect is much less noticeable for the *m*-benzporphodimethene species **7**–MX (at most 0.45 ppm), even though the  $J_{\text{CdH}}$  coupling is larger in **7**–CdCl than in **5**–CdCl, which would indicate a stronger interaction. Similarly, the drastic upfield relocation of the 22-C signals in **5**–MX species (over 20 ppm) is not fully reproduced by **7**–MX (up to 10 ppm). It should be noted that the variations of chemical shifts (especially  $^1\text{H}$ ) can be influenced by conformational and electronic effects not related to the M–arene interaction.

The magnitude of  $^1J_{\text{CH}}$  seems to be a more reliable probe for the agostic interaction. The changes in  $^1J_{\text{CH}}$  displayed by complexes **5**–MX suggest that the electron density in the CH bond is slightly depleted due to the closeness of the metal ion (coupling constant  $^1J$  is proportional to the square of the bond order).<sup>24,45</sup> The reduction in  $^1J_{\text{CH}}$  between **1** and **5**–ZnCl is ca. 9 Hz. For comparison, formation of an agostic bond in a rhodium(I) pincer complex resulted in a decrease of approximately 20 Hz.<sup>12</sup> Metal complexation has no effect on the  $^1J_{\text{CH}}$  constant in **6**–CdCl, which yields the same value of 167 Hz for  $^1J_{\text{CH}}$  couplings at the topologically equivalent positions 2,3 and 21,22.

It may be questioned whether the term “agostic”<sup>44,46</sup> should be applied to interactions involving  $d^{10}$  ions, such as Cd(II) or Hg(II). In fact, the strongest agostic bonds are formed by early transition metals with low occupancy of the 3d shell, such as titanium. There is, however, a tendency to expand the meaning of “agostic”, exemplified for instance by the cited work by Pregosin. Recently, the “s-block agostic interaction” (as opposed to the typical transition metal agostic interaction) has been described as resulting from an electrostatic attraction between dipoles and a donor–acceptor interaction between the CH bonding density and the metal cation.<sup>47</sup> Such interactions have been detected in nonsolvated oligomeric lithium derivatives,<sup>48</sup> (trimethylsilyl)silanides of the heavier alkali metals,<sup>47</sup> in a series of  $[\text{K}(\text{arene})_2]^+\text{X}^-$  and  $[\text{Rb}(\text{arene})_2]^+\text{X}^-$  species ( $\text{X} = [\text{M}(\text{N}(\text{SiMe}_3)_2)_3]^-$ ,  $\text{M} = \text{Zn}$  or  $\text{Mg}$ ),<sup>49</sup> and in nonsolvated monomeric silyl- or germyllithiums.<sup>50</sup> Close contacts, similar to those observed here for benziporphyrin complexes, were also reported by Furuta et al. for the Zn(II) complexes of N-confused

porphyrin (Zn $\cdots$ C distance of 2.42–2.49 Å)<sup>51</sup> and N-confused calix[4]phyrin (2.67 Å),<sup>52</sup> and were described as  $\eta^1$  side-on coordination. An interesting case of a Zn $\cdots$ alkene interaction has recently been reported by Anderson et al. in a chlorozinc(II) triphyrin (2.86 Å).<sup>53</sup>

It should be noted that, as the electrophilicity of the cationic center increases, the metal–arene interaction becomes stronger. In the absence of geometric restraints,  $d^{10}$  ions, such as Hg(II) and Ag(I), are capable of forming  $\pi$ -arene complexes.<sup>9–11</sup> A continuum of  $\pi$ - $\sigma$  bonds<sup>4</sup> has been observed for the more electrophilic silylium ions<sup>2</sup> or triarylaluminum species, such as  $\text{Al}(\text{C}_6\text{F}_5)_3$ .<sup>5</sup> Cd and Hg ions in the benziporphyrin environment are poor electrophiles, and hence the observed interactions are very weak. They are, however, dependent on the identity of the axial ligand, which definitely affects the electrophilicity of the metal center. Presumably, the metal–arene interaction can be further enhanced by the appropriate choice of the axial ligand and modifications of the benziporphyrin ring.

**NMR Spectra of Paramagnetic Nickel(II) Benziporphyrins.** Because of the nonplanar coordination geometry of the metal ion, the nickel complexes **5**–NiCl, **6**–NiCl, and **7**–NiCl are all paramagnetic, with  $S = 1$ . The presence of unpaired electron density greatly expands the range of observed chemical shifts and causes significant broadening of spectral lines. While the resulting spectra are well-resolved, many of the advantages of diamagnetic NMR (observation of scalar couplings, NOEs, etc.) are not always easily available. For this reason, in the analysis of paramagnetically shifted spectra, one often needs to resort to such techniques as selective deuteration or relaxation studies.

The  $^1\text{H}$  NMR spectra of **5**–NiCl and **7**–NiCl, shown in Figure 10, correspond to effective  $C_s$  symmetry of the molecule. The observed pattern of chemical shifts is quite typical for high-spin Ni(II) complexes of porphyrins and porphyrin analogues, with most of the  $\beta$ -pyrrole resonances in the downfield region of 60–10 ppm, and the *meso*-aryl peaks in the 0–10 ppm range (Table 3). Almost complete assignment of these signals is achieved with the 2D COSY spectrum. The 11,16- and 6,21-Ph substituents in **5**–NiCl have been distinguished by comparison of their dynamic behavior (relative rotation rates).

Of special interest, however, are the shifts of the *m*-phenylene protons (Table 3). Signals 2,4-H and 3-H show evident sign alteration both in **5**–NiCl (22.5 and –40.8 ppm, respectively, at 298 K) and in **7**–NiCl (28.8 and –48.1 ppm). Yet, the most unusual feature is found in the far downfield region of the spectrum. The broadened signal, which is shifted to 386 ppm in the spectrum of **5**–NiCl (298 K), is assigned to the inner 22-H. This is easily verified by acidifying a solution of compound **8**–Ni with DCl rather than HCl. The resulting species **5**–NiCl-*d* is selectively deuterated at position 22, and no low-field signal is observed. The benzporphodimethene species, **7**–NiCl, gives a signal at 208 ppm (298 K), which is assigned to 22-H by default.

The  $^1\text{H}$  NMR spectrum of the *p*-benzporphyrin complex **6**–NiCl (Figure 11) appears at first sight to be similar to the preceding spectra of **5**–NiCl and **7**–NiCl.  $\beta$ -Pyrrolic resonances take the usual downfield positions, while the *meso*-aryl reso-

(39) Anklin, C. G.; Pregosin, P. S. *Magn. Reson. Chem.* **1985**, *23*, 671.

(40) Albinati, A.; Anklin, C. G.; Ganazzoli, F.; Rüegg, H.; Pregosin, P. S. *Inorg. Chem.* **1987**, *26*, 503.

(41) Albinati, A.; Arz, C.; Pregosin, P. S. *Inorg. Chem.* **1987**, *26*, 508.

(42) Albinati, A.; Arz, C.; Pregosin, P. S. *J. Organomet. Chem.* **1988**, *356*, 367.

(43) Albinati, A.; Pregosin, P. S.; Wombacher, F. *Inorg. Chem.* **1990**, *29*, 1812.

(44) Crabtree, R. H. *Angew. Chem., Int. Ed. Engl.* **1993**, *32*, 789.

(45) Pople, J. A.; Santry, D. P. *Mol. Phys.* **1964**, *8*, 1.

(46) Brookhart, M.; Green, M. L. H. *J. Organomet. Chem.* **1983**, *250*, 395.

(47) Klinkhammer, K. W. *Chem.-Eur. J.* **1997**, *3*, 1418.

(48) Siemieling, U.; Redecker, T.; Neumann, B.; Stammeler, H.-G. *J. Am. Chem. Soc.* **1994**, *116*, 5507.

(49) Forbes, G. C.; Kennedy, A. R.; Mulvey, R. E.; Roberts, B. A.; Rowlings, R. B. *Organometallics* **2002**, *21*, 5115.

(50) Nakamoto, M.; Fukawa, T.; Lee, W. Y.; Sekiguchi, A. *J. Am. Chem. Soc.* **2002**, *124*, 15160.

(51) Furuta, H.; Ishizuka, T.; Osuka, A. *J. Am. Chem. Soc.* **2002**, *124*, 5622.

(52) Furuta, H.; Ishizuka, T.; Osuka, A. *Inorg. Chem. Commun.* **2003**, *6*, 398.

(53) Krivokapic, A.; Cowley, A. R.; Anderson, H. L. *J. Org. Chem.* **2003**, *68*, 1089.

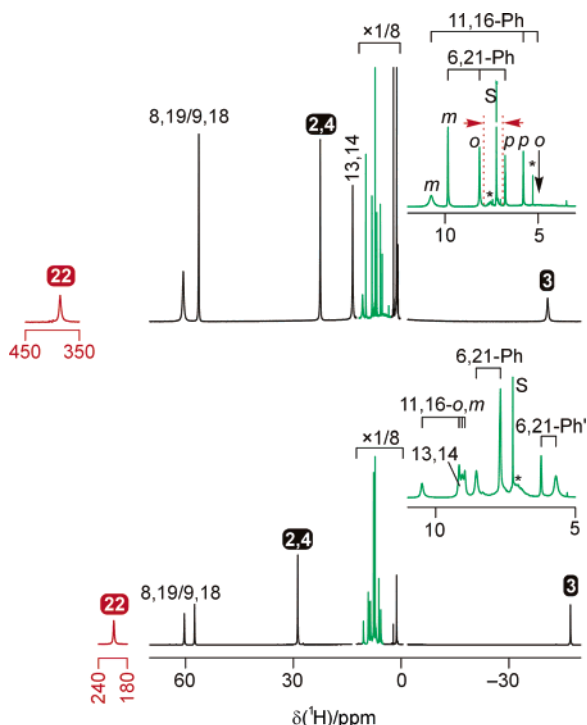


**Figure 10.**  $^1\text{H}$  NMR spectra ( $\text{CDCl}_3$ , 298 K) of complexes **5**–NiCl (top) and **7**–NiCl- $d_6$  (bottom, deuteration level ca. 60%). Insets show the expansion of the diamagnetic regions (green). The small red arrow in the upper inset marks the region containing the entire spectrum of the diamagnetic **8**–Ni (a range of ca. 1 ppm).

**Table 3.**  $^1\text{H}$  NMR Chemical Shifts ( $\delta$ /ppm) for Paramagnetic Ni(II) Benzporphyrins (298 K,  $\text{CDCl}_3$ )

signal	5–NiCl	7–NiCl	signal	6–NiCl
8,19/9,18	60.6, 56.3	60.4, 57.5	7,18/8,17	63.6, 47.2
13,14	13.5	9.2	12,13	30.5
2,4	22.5	28.8		
3	–40.8	–47.1	2,3	–10.5
22	386	208	21,22	0.0
6,21- <i>o</i> -Ph	8.1	(8.5, 7.7) <sup>a</sup> (6.2, 5.7) <sup>a</sup>	5,20- <i>o</i> -Ph	8.8
6,21- <i>m</i> -Ph	9.8		5,20- <i>m</i> -Ph	9.9
6,21- <i>p</i> -Ph	6.8		5,20- <i>p</i> -Ph	6.1
11,16- <i>o</i>	~5.2	10.5, 9.2, 9.1, 9.0	10,15- <i>o</i> -Ph	11.2, 8.0
11,16- <i>m</i>	10.8		10,15- <i>m</i> -Ph	9.6, 8.7
11,16- <i>p</i>	5.8		10,15- <i>p</i> -Ph	8.3

<sup>a</sup> The signals correspond to the two nonequivalent types of 6,21-phenyl substituents. Accidental degeneracy of certain shifts reduces the number of observed signals.

nances occupy the so-called “diamagnetic” region. The narrow upfield signal at –10.5 ppm is assigned as 2,3-H, based on its intensity and chemical shift. Further inspection of the spectrum results in the puzzling discovery of the very broad 21,22-H signal located at 0.0 ppm rather than in the far downfield region.

**Relaxation Studies.** The above assignment relies on the significant broadening of the 21,22-H signal relative to 2,3-H, which is caused by the proximity of the paramagnetic Ni(II) center. This argument can be reinforced with a quantitative analysis of relaxation times, which can yield approximate distances between the Ni ion and particular protons of the molecule.<sup>54,55</sup>  $T_1$  times are normally preferred to  $T_2$ , as they are

(54) La Mar, G. N.; Walker, F. A. *NMR of Paramagnetic Porphyrins*. In *The Porphyrins*; Dolphin, D., Ed.; Academic Press: New York, 1979; Vol. IVB, pp 57–161.

(55) Bertini, I.; Luchinat, C. *Coord. Chem. Rev.* **1996**, *150*, 1.

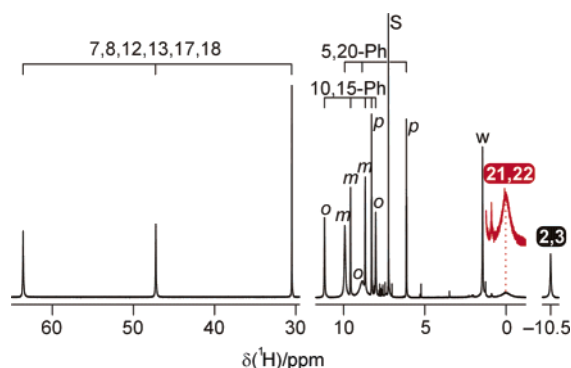


**Figure 11.**  $^1\text{H}$  NMR spectrum ( $\text{CDCl}_3$ , 298 K) of **6**–NiCl. The  $\delta$  axis of the downfield part of the spectrum is differently scaled (integral intensities are preserved).

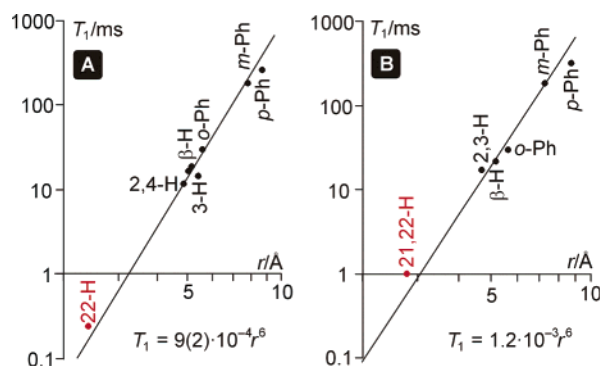


**Figure 12.** Relaxation plots for **5**–NiCl (A) and **6**–NiCl (B). The dependence between  $T_1$  ( $\text{CDCl}_3$ , 298 K) and  $r$  (crystal structure averages) is linear in bilogarithmic axes.

independent of exchange phenomena. Paramagnetically induced relaxation may be both of dipolar and of scalar origin, but the contact contribution (which can be estimated from chemical shifts) is small in the studied compounds and has been omitted in the calculations. Dipolar relaxation is expressed simply as

$$T_1 = a \cdot r^6 \quad (1)$$

where  $r$  is the distance to the paramagnetic center, and  $a$  is a constant, which is equal for all of the protons in the molecule. Furthermore, we can expect that the  $a$  values should be almost identical for **5**–NiCl and **6**–NiCl. Equation 1 leads to a linear dependence between  $T_1$  and  $r$  in bilogarithmic axes, with the slope equal to 6.

Figure 12A shows the  $T_1$  dependence on  $r$  for the *m*-benzporphyrin complex **5**–NiCl. The  $r$  values are the averages of solid-state distances. The resulting fit is fairly accurate, especially with respect to the 22-H proton. More importantly, the plot obtained for **6**–NiCl (Figure 12B) also follows a linear trend, thus confirming the assignment of 2,3-H and 21,22-H. Constants  $a$  obtained for **5**–NiCl and **6**–NiCl are indeed very similar.

**Analysis of Paramagnetic Shifts.** The similarity of spectroscopic patterns exhibited in the pyrrole and aryl regions by compounds **5**–NiCl, **6**–NiCl, and **7**–NiCl indicates a common electronic structure, so that the three systems can be treated collectively.

Convincing separation of the contact and dipolar contributions to the paramagnetic shift is required as the first step of the analysis. In the present case of the Ni(II) ion ( $d^8$ ,  $S = 1$ ), the  $g$

tensor is highly isotropic, which normally leads to negligible dipolar shifts.<sup>56</sup> However, measurable dipolar shifts can also arise as a result of zero-field splitting (ZFS). The detailed theory indicates that for high-spin  $d^8$  ions dipolar shifts arising from ZFS vary inversely with the square of the temperature ( $T^{-2}$  dependence), in contrast to the usual Curie dependence ( $T^{-1}$ ) of the contact contribution.<sup>57–59</sup> It is therefore possible, at least in principle, to separate the contact and ZFS dipolar terms by analyzing the temperature dependence of chemical shifts.

This analysis has been carried out for complexes **5**–NiCl, **6**–NiCl, and **7**–NiCl (see Table S5 and Figure S8, Supporting Information). Curie plots obtained for these species are not ideally linear and do not extrapolate to reference diamagnetic shifts, which indicates a ZFS dipolar contribution. Its magnitude has been estimated by fitting the data with the following equation

$$\delta_{\text{para}} = \alpha \cdot T^{-1} + \beta \cdot T^{-2} \quad (2)$$

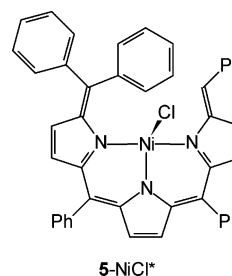
where  $\delta_{\text{para}}$  is the observed paramagnetic shift, whereas  $\alpha$  and  $\beta$  are the varied parameters. At room temperature, the dipolar contribution seldom exceeds 15%, with the exception of protons experiencing small overall shifts (0–15 ppm). It should be remembered that the above estimates are only an approximation, but exact values are not needed for the present discussion.<sup>59</sup>

An additional indication of the dominant role of the contact shift can be derived from the shift pattern of *meso*-aryl resonances. It was shown that in the paramagnetic complexes of porphyrins and their analogues this pattern depends on whether the contact or dipolar shift dominates.<sup>60</sup> In particular, the contact shift mediated by  $\pi$  orbitals of the *meso*-aryl results in a characteristic sign alteration of the shifts experienced by the *ortho*, *meta*, and *para* protons of the *meso*-phenyls. In the present case, the shift pattern displayed by *meso* substituents is compatible with the dominance of  $\pi$  contribution with only a small admixture of the dipolar shift.

Finally, to show that the observed spread of shifts is not a result of dipolar contribution, we have assumed a purely dipolar shift of 22-H and performed model calculations. By varying the orientation of the main magnetic axis in the C(22)–Ni–N(24) plane, we have arrived at a range of orientations (tilt of 0–30° with respect to Ni–Cl bond) that yield acceptable shift values for protons 2,4-H and 3-H. These orientations, however, provide unreasonably large dipolar shifts for all of the remaining positions (an order of magnitude larger than the experimental values of paramagnetic shift). As a consequence, dipolar mechanism does not account for the observed magnitude of 22-H shifts in **5**–NiCl and **7**–NiCl.

Downfield shifts of  $\beta$ -pyrrole resonances in **5**–NiCl, **6**–NiCl, and **7**–NiCl indicate  $\sigma$ -delocalization of spin density. This is consistent with the ground state of Ni(II), which has two unpaired electrons in the  $\sigma$ -symmetry orbitals ( $d_{x^2-y^2}$ )( $d_{z^2}$ )<sup>1</sup>. The spread of the pyrrole resonances is, however, significant, large

Scheme 5



differences in contact shifts being observed even for protons located on the same pyrrole ring. This suggests that  $\pi$ -delocalization is also involved, which is probably a result of mixing the  $\sigma$  and  $\pi$  orbitals due to the nonplanarity of the macrocycle. Similar effects were observed previously in the paramagnetic Ni(II) of *N*-methylporphyrin,<sup>59</sup> thiaporphyrin,<sup>61</sup> and *C*-methylated *N*-confused porphyrin.<sup>28</sup>

**Metal–Arene Interaction in the Paramagnetic Ni(II) Benzporphyrins.** The relationship between metal–arene interaction and paramagnetic shifts of the phenylene protons in Ni(II) benzporphyrins requires special consideration. The main questions that need to be answered are: (1) how is the spin density transferred to the *m*-phenylene protons in **5**–NiCl and **7**–NiCl, and (2) why are the shift patterns exhibited by *m*- and *p*-phenylene so different?

While it is natural to think of the enormous 22-H shift in **5**–NiCl as originating from a direct interaction between the paramagnetic Ni(II) ion and the arene ring, the possibility of indirect through-bond delocalization along the macrocyclic frame cannot be immediately ruled out. Comparison of phenylene shifts in compounds **5**–NiCl and **7**–NiCl shows that the values for 2,4-H and 3-H are very similar, while the 22-H shift has a large positive value in both cases, even though it is significantly reduced in **7**–NiCl. However, 22-H lies very close to the Ni(II) center, and its shift may be profoundly influenced by only slight conformational differences between **5**–NiCl and **7**–NiCl. We can therefore conclude that the phenylene shifts are rather insensitive to the geometry of 6,21-*meso* bridges (trigonal in **5**–NiCl and tetrahedral in **7**–NiCl), which means that the indirect transfer of spin density does not significantly affect the observed shift pattern.

To gain further insight into the possibility of indirect delocalization, we can imagine a **5**–NiCl molecule dissected at the C(5)–C(6) bond (**5**–NiCl\*) (Scheme 5). In such a system, the former *m*-phenylene ring simply becomes a phenyl substituent, topologically equivalent to the 21-Ph group. It follows that the indirect shifts of the phenylene may be of magnitude similar to that of the shifts of *meso* substituents. It should be noted, however, that the phenylene has two points of attachment, and a fixed orientation with respect to the macrocycle.

The paramagnetic shifts induced in the *m*-phenylene fragment are therefore mainly of contact origin with a direct delocalization of spin density onto the ring. This density can be transferred according to several different mechanisms (Figure 13).

The first possibility involves donation of electron density from the  $\sigma$ -bonding orbital of the C(22)–H bond to the half-occupied  $d_{x^2-y^2}$  orbital of nickel(II), leaving positive spin density on the

(56) *NMR of Paramagnetic Molecules. Principles and Applications*; La Mar, G. N., Horrocks, W. D., Jr., Holm, R. H., Eds.; Academic Press: New York, 1973.

(57) Kurland, R. J.; McGarvey, B. R. *J. Magn. Reson.* **1970**, *2*, 286.

(58) Bleaney, B. J. *J. Magn. Reson.* **1972**, *8*, 91.

(59) Latos-Grażyński, L. *Inorg. Chem.* **1985**, *24*, 1681.

(60) Walker, F. A. Proton NMR and EPR Spectroscopy of Paramagnetic Metalloporphyrins. In *The Porphyrin Handbook*; Kadish, K. M., Smith, K. M., Guilard, R., Eds.; Academic Press: San Diego, CA, 2000; Vol. 5, Chapter 36, pp 81–183.

(61) Latos-Grażyński, L.; Lisowski, J.; Olmstead, M. M.; Balch, A. L. *Inorg. Chem.* **1989**, *28*, 7348.

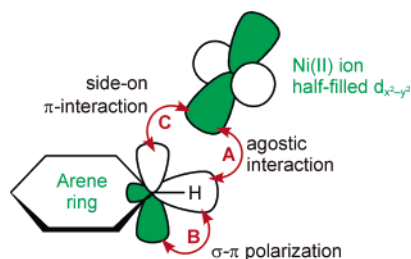


**Figure 13.** Possible routes of spin density delocalization between the Ni(II) ion and phenylene in paramagnetic nickel benziporphyrins.

CH fragment (route A, Figure 13). This corresponds to the formation of an agostic bond, which has actually been observed in the crystal structure of **5**-NiCl. This agostic mechanism must be operative, because it is the only one to account for the observed large 22-H shifts (see below).

The shifts of protons 2,4-H and 3-H can be rationalized in terms of a two-step mechanism (route A+B). Positive spin density is initially introduced via the agostic bond. The CH bond polarizes the adjacent  $p_z$  orbital to yield negative density, which is then distributed in the  $\pi$  system of the arene by means of internal polarization. This mechanism, which is typical of aromatic systems, results in alternation of spin density signs on adjacent carbon atoms.<sup>62,63</sup> Finally, the  $\pi$  system polarizes the remaining CH bonds. The positive 22-H shift would induce a positive shift of 2,4-H and a negative shift of 3-H, which agrees with the experimental observations. However, for the two-step mechanism, the 2,4-H and 3-H chemical shifts would be expected to approximately scale with the value of the 22-H shift. As shown before, no such trend is observed for **5**-NiCl and **7**-NiCl; the significant reduction in the 22-H shift of the latter species has no effect on the values for 2,4-H and 3-H.

Spin density may also be introduced into the  $\pi$  system of the arene in a direct interaction with the unpaired electrons of Ni(II) (route C) and then distributed in the phenylene moiety similar to that described above for route B. However, the sign of the spin density in the  $p_z$  orbital of 22-C should be positive. As a consequence, the expected signs of proton shifts will be opposite those predicted for route B (negative for 22-H and 2,4-H, and positive for 3-H).

While we are unable to establish relative contributions of routes B and C to the observed 2,4-H and 3-H shifts, the shift of 22-H is certainly dominated by the agostic mechanism of spin delocalization (route A). If we assume that the 22-H shift originates from polarization of the CH bond by the  $\pi$  system, we can use the McConnell formula to estimate the spin density on the adjacent carbon.<sup>56</sup> For **5**-NiCl, we obtain  $\rho_{22-C} = -0.15$ . This value seems unnaturally large, especially for the weak metal-arene interaction under study.<sup>56</sup> Finally, if  $\pi$  transfer were indeed the only active mechanism of spin delocalization, the magnitude of 2,4-H and 3-H shifts would be comparable to the shift of 22-H, which is not observed.

It follows from the above analysis that the paramagnetic shift of the internal 22-H proton is principally due to the metal-arene agostic interaction. To account for the shifts of protons 2,4-H and 3-H, it is necessary to assume  $\pi$  delocalization in

the arene ring, which may result either from direct interaction with the metal center or from  $\sigma$ - $\pi$  polarization. This polarization is induced by the spin density contained in the agostic CH bond or, to a lesser extent, in the tripyrrolic brace.

The above model provides a plausible explanation of the extraordinary shift experienced by protons 21,22-H of the *p*-benzporphyrin species, **6**-NiCl. The X-ray structure of this complex has shown that the agostic interaction is ineffective, a result of the different orientation of the arene with respect to the Ni(II) ion. Assuming that the direct spin transfer to the CH bonds is no longer possible, we are left with the much less efficient mechanisms involving polarization of the  $\pi$  system. The unusual 0 ppm shift of 21,22-H may result from accidental cancellation of small opposing effects.

$M \cdots HC$  agostic interactions were previously observed in Mn(II) and Fe(II) complexes of N-confused porphyrin. In the three structurally characterized Mn(II) species, the  $M \cdots C$  distance is 2.407(6) Å (cyclic dimer),<sup>64</sup> 2.357(5) Å (monomer, axial pyridine),<sup>64</sup> and 2.437(7) Å (monomer, axial bromide, protonated external nitrogen).<sup>65</sup> A particularly strong agostic interaction was discovered for bromoiron(II) N-confused porphyrin ( $Fe \cdots C$  of 2.36(1) Å and  $Fe \cdots H$  of 1.97 Å).<sup>66</sup> This compound can be transformed into a cyclic dimer with a comparable  $Fe \cdots C$  distance of 2.341(5) Å.<sup>67</sup> Recently, the bromoiron(II) species has been shown to exhibit an enormous 21-H shift of 812 ppm (298 K).<sup>68</sup> This result is in full agreement with the agostic mechanism of spin density transfer proposed here.

Interestingly, all known Ni(II) complexes of N-confused porphyrin protonated on the internal carbon (21-C) are diamagnetic.<sup>69–71</sup> However, the 21-C-methylated species are paramagnetic and exhibit large <sup>1</sup>H shifts of the 21-methyl group (ca. 110 ppm for the chloride complex).<sup>28,72–74</sup> These values were explained in terms of  $\sigma$ -delocalization via the  $Ni \cdots C-C-H$  bond path<sup>28</sup> or of a dipolar contribution.<sup>72</sup> However, we have noticed that the  $M \cdots H$  distances between the Ni(II) center and the 21 substituent can be small enough to form an agostic bond. The agostic mechanism can therefore be proposed as an additional contribution to the 21-CH<sub>3</sub> and 21-CH<sub>2</sub> shifts, as it leads to large positive shift values and is distance- and orientation-dependent.

**AIM Analysis of Cd(II) Benziporphyrins.** The observation of scalar coupling between the Cd nucleus and arene protons in **5**-CdCl, **6**-CdCl, and **7**-CdCl indicates that there must be a certain accumulation of electron density between the metal and arene to transmit the coupling. However, NMR data do not explain the nature of the metal-arene interaction. It might be regarded as a sterically compressed van der Waals interaction, but it might as well have some bonding character. The following computational work is an attempt to answer this question.

- (64) Harvey, J. D.; Ziegler, C. J. *Chem. Commun.* **2002**, 1942.  
 (65) Bohle, D. S.; Chen, W.-C.; Hung, C.-H. *Inorg. Chem.* **2002**, *41*, 3334.  
 (66) Chen, W.-C.; Hung, C.-H. *Inorg. Chem.* **2001**, *40*, 5070.  
 (67) Hung, C.-H.; Chen, W.-C.; Lee, G.-H.; Peng, S.-M. *Chem. Commun.* **2002**, 1516.  
 (68) Rachlewicz, K.; Wang, S.-L.; Peng, C.-H.; Hung, C.-H.; Latos-Grażyński, L. *Inorg. Chem.* **2003**, *42*, 7348.  
 (69) Lash, T. D.; Richter, D. T.; Shiner, C. M. *J. Org. Chem.* **1999**, *64*, 7973.  
 (70) Schmidt, I.; Chmielewski, P. J. *Tetrahedron Lett.* **2001**, *42*, 6389.  
 (71) Chmielewski, P. J.; Latos-Grażyński, L.; Schmidt, I. *Inorg. Chem.* **2000**, *39*, 5475.  
 (72) Schmidt, I.; Chmielewski, P. J. *Inorg. Chem.* **2003**, *42*, 5579.  
 (73) Chmielewski, P. J.; Latos-Grażyński, L. *Inorg. Chem.* **2000**, *39*, 5639.  
 (74) Schmidt, I.; Chmielewski, P. J. *Chem. Commun.* **2002**, 92.

(62) Chmielewski, P. J.; Latos-Grażyński, L.; Rachlewicz, K. *Magn. Reson. Chem.* **1993**, *31*, S47.

(63) Arasasingham, R. D.; Balch, A. L.; Hart, R. H.; Latos-Grażyński, L. *J. Am. Chem. Soc.* **1990**, *112*, 7566.

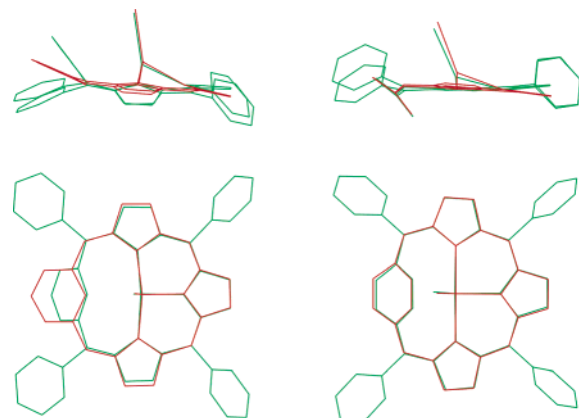


**Figure 14.** Comparison of X-ray and DFT geometries (green and red, respectively) for structures **5**–CdCl/**5'**–CdCl (left) and **6**–CdCl/**6'**–CdCl (right).

The theory of atoms in molecules (AIM) developed by Bader<sup>75</sup> derives chemically relevant information from the topology of electron density in a molecule (see the Experimental Section for a summary of basic concepts). In particular, it is capable of describing chemical bonding in terms of bond critical points (BCPs) and bond paths, and provides an unambiguous scheme of partitioning molecules into “atoms” (atomic basins).

Calculations have been performed for cadmium complexes of *m*- and *p*-benzoporphyrin, **5'**–CdCl and **6'**–CdCl, with aryl substituents replaced by hydrogens to reduce computational effort ( $R^1 = R^2 = H$ ). The two DFT-optimized structures (B3LYP/LANL2DZ) are very similar to the X-ray geometries, except for the orientation of the *m*-phenylene ring in **5'**–CdCl (Figure 14, see also Table S6, Supporting Information). This ring is closer to coplanarity with the  $N_3$  plane in the DFT model than in the crystal structure, the  $C_6/N_3$  interplanar angles being  $23^\circ$  and  $52^\circ$ , respectively. This difference is probably caused by the absence of *meso*-aryl substituents rather than by deficiencies of the calculation method, and reflects the inherent flexibility of the *m*-benzoporphyrin ligand. As a result of the different phenylene tilt, the  $Cd\cdots C(22)$  and  $Cd\cdots H(22)$  distances in the DFT structure become 2.88 and 2.46 Å (mean values in the X-ray structure are 2.72 and 2.67 Å, respectively). Apparently, the DFT structure overemphasizes the agostic character of the Cd–arene interaction. However, we have decided to use this DFT model of **5'**–CdCl for the AIM analysis because the X-ray geometry does not correspond to a numerical energy minimum, which is required by the theory of AIM.<sup>75</sup>

Figure 15 shows the connectivity of critical points in structures **5'**–CdCl and **6'**–CdCl, as well as important cross sections of the electron density. Numerical properties of selected critical points are given in Table 4 (see Supporting Information for additional data). The topology of electron density in **5'**–CdCl agrees with chemical expectations (Figure 15A): each BCP is associated with a bond, and there are eight ring points (benzene ring, three pyrrole rings, and the four inner rings formed upon binding of cadmium). Most importantly, there is a bond critical point between the Cd(II) ion and arene. The bond path passing through this point connects cadmium and C(22) (Figure 15B). The path strongly bends towards the carbon, suggesting that the interaction is topologically unstable.<sup>75</sup> This

particular shape of the bond path and the vicinity of the C(22)/H(22) boundary imply that the metal–arene pair approaches a conflict structure, in which the bond path connects to the BCP of the C(22)–H(22) bond. Such a conflict structure may collapse either into a Cd–C bond or into a Cd–H bond. These two topologies may therefore be interconvertible via only small conformational changes.

Popelier and Logothetis observed significant bending of M–H bond paths in a study of agostic bonds in  $RTiCl_2^+$  ( $R = Et, Pr$ ).<sup>76</sup> In one case, the bond path approached a conflict structure similar to that proposed for **5'**–CdCl. Curved bond paths were also characteristic of intermolecular interactions studied by Bone and Bader.<sup>77</sup>

The topology of electron density calculated for **6'**–CdCl shows several unexpected features (Figure 15C,D). The metal–arene interaction leads to a conflict structure enforced by molecular symmetry ( $C_s$ ). The BCP between cadmium and arene lies on the plane of symmetry, and the corresponding bond path connects the Cd nucleus with the BCP of the C(21)–C(22) bond (Figure 15D). Similar conflict structures were observed in  $\pi$ -bonded hydrogen complexes of HF with acetylene and ethylene.<sup>78</sup>

Additional features of the electron density in **6'**–CdCl are a result of steric congestion (it should be remarked the steric interactions accompanied by bond paths are not repulsive according to the AIM theory).<sup>79</sup> Two equivalent bond paths, C(22)–N(23) and C(21)–N(25), connect the phenylene with inner nitrogens, leading to an increase in the number of ring critical points. The ring points lie fairly close to the [22,23] and [21,25] BCPs, indicating that the accumulation of density is not significant. Finally, two ring points and a cage point have been found in the space between the arene ring and the chloride (see also Figure S9, Supporting Information). To satisfy the Poincaré–Hopf relationship, one must assume the presence of yet another BCP, which could not be recovered by the software. This BCP lies between the Cl nucleus and the BCP of the C(2)–C(3) bond, and the corresponding bond path closes a cage structure.

Comparison of the properties of various bond critical points is helpful in discussing the metal–arene interaction in cadmium benzoporphyrins. The data gathered in Table 4 provide examples of a typical covalent bond (C–C), bonds with high degree of ionicity (Cd–N and Cd–Cl), steric congestion ( $C\cdots N$ ), and the metal–arene interaction itself ( $Cd\cdots C$ ). Evidently, the metal–arene interaction only has a weakly bonding character. The densities  $\rho$  at the respective BCPs in **5'**–CdCl and **6'**–CdCl do not exceed 0.02 au and are only slightly larger than the  $\rho$  values obtained for  $C\cdots N$  interactions in **6'**–CdCl. Correspondingly, bond orders  $B$  calculated for the  $Cd\cdots C$  contacts according to the Mayer method<sup>80</sup> (0.077 for **5'**–CdCl and 0.064 for **6'**–CdCl) are significantly lower than the Cd–N and Cd–Cl bond orders. The  $Cd\cdots H(22)$  bond order in **5'**–CdCl is even lower (0.0317).

The  $Cd\cdots$ arene BCPs in **5'**–CdCl and **6'**–CdCl show large ellipticities (0.97 and 2.32, respectively). In comparison, the C(13)–C(14) bonds have  $\epsilon$  values of ca. 0.2, typical for a

(75) Bader, R. F. W. *Atoms in Molecules – a Quantum Theory*; Oxford University Press: Oxford, 1990.

(76) Popelier, P. L. A.; Logothetis, G. *J. Organomet. Chem.* **1998**, 555, 101.

(77) Bader, R. F. W. *J. Phys. Chem.* **1996**, 100, 10892.

(78) Tang, T. H. *THEOCHEM* **1990**, 207, 319.

(79) Bader, R. F. W. *J. Phys. Chem. A* **1998**, 102, 7314.

(80) Angyan, J. G.; Loos, M.; Mayer, I. *J. Phys. Chem.* **1994**, 98, 5244.

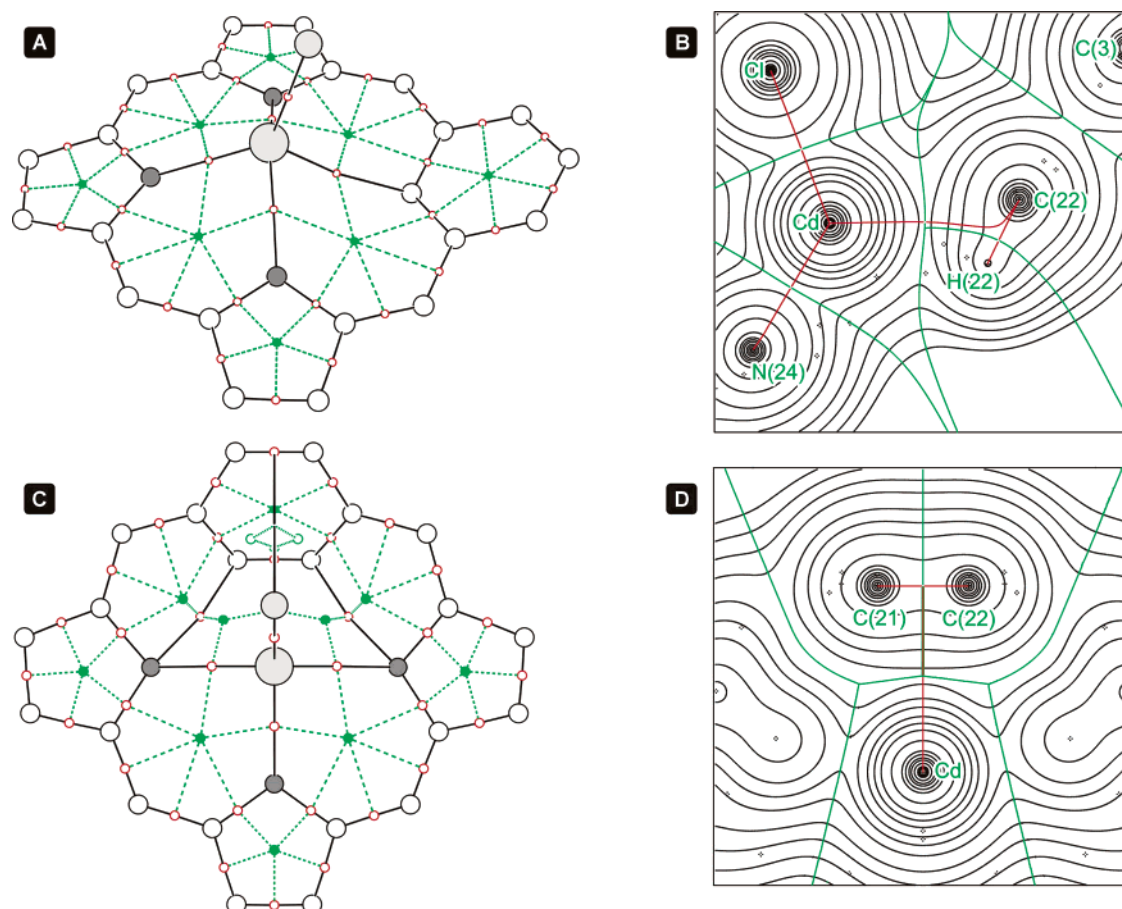


**Figure 15.** Connectivity of critical points in the theoretical electron densities of  $5'$ -CdCl (A) and  $6'$ -CdCl (B). The hydrogen (3, -3) points and BCPs of the C–H bonds are omitted for clarity. Bond critical points are shown in red. Black lines are approximations of bond paths. Ring critical points and their connectivity (dashed lines) are shown in green. Parts B and D show the electron density distributions in  $5'$ -CdCl (in the symmetry plane) and  $6'$ -CdCl (in the plane of atoms Cd, C(21), and C(22)). Green and red lines denote boundaries of atomic basins and bond paths, respectively.

**Table 4.** Parameters of Selected Bond Critical Points (BCPs) Obtained from the AIM Analyses of  $5'$ -CdCl and  $6'$ -CdCl (In au or Dimensionless)<sup>a</sup>

	$5'$ -CdCl					$6'$ -CdCl				
	$\rho$	$\nabla^2\rho$	$H$	$\epsilon$	$B$	$\rho$	$\nabla^2\rho$	$H$	$\epsilon$	$B$
Cd $\cdots$ C(22)	0.0186	0.0637	-0.0002	0.9703	0.0773					0.0638 <sup>c</sup>
Cd $\cdots$ [21,22] <sup>b</sup>						0.0180	0.0566	-0.0003	2.3216	0.0638 <sup>c</sup>
Cd–N(24)	0.0639	0.3103	-0.0066	0.0846	0.3530	0.0658	0.3211	-0.0069	0.0876	0.3719
Cd–N(23)	0.0548	0.2433	-0.0056	0.0897	0.3246	0.0518	0.2213	-0.0055	0.0815	0.3058
Cd–N(25)	0.0548	0.2427	-0.0057	0.0914	0.3270	0.0518	0.2213	-0.0054	0.0813	0.3050
Cd–Cl	0.0536	0.1848	-0.0075	0.0004	0.6146	0.0526	0.1793	-0.0074	0.0044	0.5829
C(13)–C(14)	0.3044	-0.8291	-0.3215	0.2188	1.6495	0.3022	-0.8197	-0.3169	0.2110	1.6140
C(22) $\cdots$ N(23)						0.0146	0.0563	0.0020	0.6452	0.0521
C(21) $\cdots$ N(25)						0.0146	0.0563	0.0020	0.6434	0.0521

<sup>a</sup> Explanation of symbols:  $\rho$ , electron density at BCP;  $\nabla^2\rho$ , Laplacian;  $H$ , total energy density;  $\epsilon$ , ellipticity;  $B$ , bond order according to Mayer et al.<sup>80</sup> <sup>b</sup> [21,22] is the BCP between atoms C(21) and C(22) (see text for explanation). <sup>c</sup> Bond orders for Cd $\cdots$ C(21) and Cd $\cdots$ C(22).

C(sp<sup>2</sup>)–C(sp<sup>2</sup>) bond.<sup>75</sup> The large  $\epsilon$  values indicate that the absolute value of  $\lambda_2$  is small; that is, the electron density profile along the direction of the corresponding eigenvector ( $l_2$ ) is rather flat. BCPs with high  $\epsilon$  values are therefore associated with structural instabilities.<sup>81</sup> Indeed, inspection of the Hessians shows that in the case of the Cd–arene BCP in  $5'$ -CdCl the  $l_2$  vector is directed approximately parallel to the C(22)–H(22) bond, whereas in  $6'$ -CdCl it is parallel to the C(21)–C(22) bond.

A unique feature of AIM is that it is able to quantify the degree of electron sharing. The most commonly used measure

is the Laplacian of electron density  $\nabla^2\rho$  in conjunction with the  $\rho$  value at a bond critical point.<sup>77</sup> Covalent bonds (shared interactions) are characterized by  $\rho$  values exceeding 0.1 au, while  $\nabla^2\rho$  can be negative (nonpolar bonds) or positive (certain polar bonds, such as C=O). For ionic bonds, H-bonds, and in van der Waals molecules (closed-shell interactions), the density  $\rho$  is in the range  $10^{-3}$ – $10^{-2}$  au, while the Laplacian is always positive. In this sense, agostic bonds are of the closed-shell type ( $\rho = 0.04$ – $0.05$  au,  $\nabla^2\rho = 0.15$ – $0.25$  au).<sup>76</sup>

The values given in Table 4 agree with the literature observations. The Cd–N and Cd–Cl bonds are largely ionic, in contrast to the covalent bonds of the macrocycle, as

(81) Popelier, P. L. A. *Atoms in Molecules. An Introduction*; Pearson Education: Harlow, 2000.

exemplified by C(13)–C(14). The Cd⋯arene and C⋯N interactions are characterized by similar values of  $\rho$  and  $\nabla^2\rho$ , comparable to the results obtained for hydrogen bonds.<sup>81</sup>

A complementary parameter proposed to classify bonding types is the total electronic energy density  $H$  at the BCP.<sup>82</sup> Negative values have been associated with electron sharing, and positive values have been associated with closed-shell interactions. With the exception of C⋯N interactions, all  $H$  values given in Table 4 are negative. However, the absolute values of  $H$  obtained for Cd⋯arene interactions and ionic bonds are very small, so that the degree of electron sharing must be considered insignificant.

## Conclusion

The combination of structural motifs in benziporphyrins provides a unique opportunity to study weak metal–arene interactions. The metal ion, bound by the tripyrrolic brace, is brought into the vicinity of the arene, and the resulting complex can be investigated by spectroscopic methods or X-ray crystallography. The tripyrrolic fragment inherits much of the versatility of the parent porphyrin ligand, so that a variety of metal ions can be coordinated. The properties of the complex can be fine-tuned by peripheral substitution and judicious choice of the axial ligand.

In the present paper, we have described spectroscopic manifestations of the metal–arene interactions observed in the diamagnetic Zn(II), Cd(II), and Hg(II) benziporphyrin complexes and in the paramagnetic Ni(II) species. Three macrocycles have been used: *m*-benziporphyrin, its *para* isomer, and the newly synthesized *m*-benziporphodimethene, designed so as to provide different orientations of the arene with respect to the coordination center and different linkages between the arene fragment and the rest of the macrocycle.

In the diamagnetic systems, the metal–arene interaction leads to scalar coupling between the spin-active metal nucleus (<sup>111</sup>Cd, <sup>113</sup>Cd, and <sup>199</sup>Hg) and the proximate <sup>1</sup>H and <sup>13</sup>C nuclei of the arene. The couplings are transmitted despite the absence of a formal M–arene bond, and their magnitude is dependent on geometric factors (position of the metal ion with respect to the arene) and electronic factors (identity of the axial ligand).

In the Ni(II) complexes, unusual paramagnetic shifts are observed for the arene protons close to the metal center. These shifts are explained by an agostic mechanism of spin density transfer, in which electron donation from the CH bond to the metal is responsible for spin delocalization. The agostic mechanism is vindicated by an analysis of paramagnetic shifts and the available structural data. The position of the metal relative to the CH bond has a great impact on the observed shift, as is evident from the comparison of *meta*- and *para*-benziporphyrins species (**5**–NiCl and **6**–NiCl).

It is difficult to draw parallels between scalar coupling and contact shift even though the two phenomena have a common physical source. The difference in paramagnetic shifts between **5**–NiCl and **6**–NiCl indicates that the agostic mechanism of spin density transfer has a more directional character or is more distance-dependent than the scalar couplings observed in **5**–CdCl and **6**–CdCl. In fact, the AIM analysis shows that the metal–arene interactions in **5**–CdCl and **6**–CdCl are of similar

strength, while the differences in agostic bonding between **5**–NiCl and **6**–NiCl are quite significant.

When the contribution of agostic mechanism to the overall paramagnetic shift is small, it is effectively masked by other scalar or dipolar mechanisms, and therefore difficult to unravel. In contrast, through-bond contributions to the observed metal–arene scalar couplings are negligible in the studied systems, so that the observed effect can wholly be ascribed to a direct interaction.

It appears that the interaction could be significantly amplified by increasing the electron density on the arene and the positive charge on the metal ion. Systematic investigation of appropriately modified systems may help in quantifying the relationship between bonding strength and the spectroscopic probes described in this paper.

## Experimental Section

Dichloromethane and acetonitrile were distilled from calcium hydride prior to use. Nickel(II) chloride was dried at 200 °C until yellow. Anhydrous cadmium(II) chloride was prepared according to a literature procedure.<sup>83</sup> Anhydrous zinc(II) chloride and mercury(II) chloride were used as received.

**6,11,16,21-Tetraphenyl-*m*-benziporphyrin (1)<sup>18</sup> and 5,10,15,20-tetraphenyl-*p*-benziporphyrin (2)<sup>19</sup>** were obtained as previously described.

**1,3-Bis(diphenylhydroxymethyl)benzene (4)**. Dimethyl isophthalate (1.94 g, 10 mmol) is dissolved in 150 mL of dry degassed THF. PhMgBr (44 mL of a 1 M solution in Et<sub>2</sub>O, 44 mmol) is added. After being stirred for 1 h, the reaction mixture is hydrolyzed with aqueous ammonium chloride and extracted with CH<sub>2</sub>Cl<sub>2</sub>. The extracts are washed twice with water, and the solvent is removed under reduced pressure. Compound **4** is isolated as a yellowish viscous oil slowly crystallizing on standing. Yield: approximately 80%. <sup>1</sup>H NMR (CDCl<sub>3</sub>, 298 K, numbering corresponds to that of **3**): 7.49 (t, 1H, 22-H), 7.15–7.35 (m, 23H, 6,6,21,21-Ph, 2,4-H, 3-H), 3.25 (b, 2H, OH). <sup>13</sup>C NMR (CDCl<sub>3</sub>, 298 K, partial data): 146.6 (6,6,21,21-*i*-Ph), 146.4 (1,5-C), 127.8 (22-C), 126.7 (2,4-C), 82.0 (5,21-C).

**11,16-Bis(4-nitrophenyl)-6,6,21,21-tetraphenyl-*meta*-benzi-6,21-porphodimethene (3)**. Precursor **4** (1 mmol, 442 mg), pyrrole (3 mmol, 208 μL), and 4-nitrobenzaldehyde (302 mg, 2 mmol) are added to dry CH<sub>2</sub>Cl<sub>2</sub> (900 mL). Oxygen is removed by bubbling nitrogen gas through the solution for 15 min. The vessel is then sealed with septum caps, and Et<sub>2</sub>O:BF<sub>3</sub> (100 μL) is added. The solution is protected from light and stirred for 2 h. After this time, DDQ (2 mmol, 454 mg) is added and dissolved by continuous stirring, and the reaction mixture is evaporated under reduced pressure. The residue is chromatographed (column 5 × 20 cm, grade II basic alumina Al<sub>2</sub>O<sub>3</sub>, CH<sub>2</sub>Cl<sub>2</sub>) to yield **3** as the first fraction (a trace of tetrakis(4-nitrophenyl)porphyrin elutes immediately after **3**). Crude **3** is purified by crystallization (CH<sub>2</sub>Cl<sub>2</sub>/MeOH), forming a fleecy red precipitate. Yield: 117 mg (14%). <sup>1</sup>H NMR (CDCl<sub>3</sub>, 313 K): 12.27, 5.93 (AB<sub>2</sub>: 24-H, 13,14-H, <sup>4</sup>J<sub>AB</sub> = 1.8 Hz); 8.24, 7.58 (AA'BB': 11,16-*m*, 11,16-*o*, <sup>3</sup>J<sub>AB</sub> = 8.8 Hz); 7.68, 7.09, 7.05 (ABC<sub>2</sub>: 22-H, 3-H, 2,4-H, <sup>4</sup>J<sub>AC</sub> = 1.7 Hz, <sup>3</sup>J<sub>BC</sub> ≈ 7.8 Hz); 7.23–7.11 (m, 20H, 6,6,21,21-Ph); 6.48, 6.45 (AB: 9,18-H, 8,19-H, <sup>3</sup>J<sub>AB</sub> = 4.7 Hz). <sup>13</sup>C NMR (CDCl<sub>3</sub>, 313 K): 180.7 (7,20-C); 152.3 (10,17-C); 148.2 (11,16-*p*); 145.3 (1,5-C); 145.1 (6,6,21,21-*i*-Ph); 145.0 (11,16-*i*); 138.4 (12,15-C); 136.1 (22-C); 134.2 (11,16-C); 134.1 (9,18-C); 132.1 (11,16-*o*); 130.6 (8,19-C); 130.2 (6,6,21,21-*o*-Ph); 127.9 (6,6,21,21-*m*-Ph); 126.9 (2,4-C); 126.2 (3-C); 126.1 (6,6,21,21-*p*-Ph); 122.8 (11,16-*m*); 121.0 (13,14-C); 64.1 (6,21-C). UV–vis (CH<sub>2</sub>Cl<sub>2</sub>, λ<sub>max</sub> [nm] (log ε)): 328 (4.63), 529 (4.28), 565 (4.32). HRMS (ESI, *m/z*): 870.3103 (870.3075 for C<sub>58</sub>H<sub>39</sub>N<sub>5</sub>O<sub>4</sub> + H<sup>+</sup>).

(82) Cremer, D.; Kraka, E. *Angew. Chem., Int. Ed. Engl.* **1984**, *23*, 627.

(83) *Handbook of Preparative Inorganic Chemistry*, 2nd ed.; Bauer, G., Ed.; Academic Press: New York, London, 1963.

Pyrrole-deuterated ligands **1-d<sub>6</sub>**, **2-d<sub>6</sub>**, and **3-d<sub>6</sub>** were obtained using pyrrole-d<sub>5</sub> (Aldrich, 98% D). The observed isotopic enrichment was ca. 50–60% D only, a result of proton–deuteron exchange during condensation.

**Zinc(II) Insertion (General Procedure for 5–ZnCl, 6–ZnCl, 7–ZnCl).** The respective benzporphyrin (**1**, **2**, or **3**, 20 mg) and anhydrous zinc(II) chloride (molar excess) are added to acetonitrile (15 mL) and refluxed under nitrogen for 15 min. The reaction mixture is then cooled and diluted with water to remove excess ZnCl<sub>2</sub>. The product is extracted with dichloromethane, and the extracts are dried with anhydrous sodium sulfate and evaporated to dryness. The residue contains practically pure chlorozinc complex.

**Chlorozinc(II) 6,11,16,21-Tetraphenyl-*m*-benzporphyrin (5–ZnCl).** <sup>1</sup>H NMR (CDCl<sub>3</sub>, 298 K): 7.55–7.40 (m, 6,11,16,21-Ph); 7.65, 7.12, 5.51 (AB<sub>2</sub>C: 3-H, 2,4-H, 22-H, <sup>3</sup>J<sub>AB</sub> = 7.8 Hz, <sup>4</sup>J<sub>BC</sub> = 1.7 Hz); 7.50, 6.83 (AB: 8,19-H, 9,18-H <sup>3</sup>J = 5.1 Hz), 6.99 (s, 13,14-H). <sup>13</sup>C NMR (CDCl<sub>3</sub>, 298 K): 170.5 (10,17-C); 161.0 (12,15-C); 153.4 (7,20-C); 141.9 (6,21-C); 141.8 (6,21/11,16-*i*-Ph); 139.6 (6,21/11,16-*i*-Ph); 139.4 (1,5-C); 136.3 (8,19-C); 134.0 (13,14-C); 133.6 (6,21/11,16-*o*-Ph); 132.9 (3-C); 132.5 (6,21/11,16-*o*-Ph); 131.9 (2,4-C); 131.8 (9,18-C); 129.0 (6,21/11,16-*m*-Ph); 127.8 (6,21/11,16-*m*-Ph); 127.6 (6,21/11,16-*p*-Ph); 127.5 (6,21/11,16-*p*-Ph); 116.6 (11,16-C); 85.8 (22-C). HRMS (ESI, *m/z*): 688.1754 (688.1726 for C<sub>46</sub>H<sub>30</sub>N<sub>3</sub>Zn<sup>+</sup>).

**Chlorozinc(II) 5,10,15,20-Tetraphenyl-*p*-benzporphyrin (6–ZnCl).** <sup>1</sup>H NMR (CDCl<sub>3</sub>, 298 K): 8.66, 8.31 (AB: 7,18-H, 8,17-H, <sup>3</sup>J = 4.8 Hz); 8.38, 1.33 (AA'BB': 2,3-H, 21,22-H, <sup>3</sup>J<sub>AA'} ≈ 7.5 Hz, <sup>4</sup>J<sub>AB} ≈ 2.0 Hz); 8.14 (b, 4H, 5,20-*o*-Ph); 8.27 (s, 2H, 12,13-H); 8.10, 7.87 (2 × m, 4H, 10,15-*o*-Ph); 7.74 (~t, 4H, 5,20-*m*-Ph); 7.70–7.69 (m, 8-H, 5,20-*p*-Ph, 10,15-*m,p*-Ph). <sup>13</sup>C NMR (CDCl<sub>3</sub>, 298 K): 158.8 (9,16-C); 155.8 (1,4-C); 155.1 (6,19-C); 154.4 (11,14-C); 144.3 (5,20-C); 142.3 (10,15-*i*-Ph); 140.2 (5,20-*i*-Ph); 136.5 (5,20-*o*-Ph); 134.9 (7,18-C); 134.7 (8,17-C); 134.6 (10,15-*o*-Ph); 134.0 (12,13-C); 133.4 (10,15-*o*-Ph); 133.1 (21,22-C); 131.1 (2,3-C); 128.8 (*m/p*-Ph); 128.3 (*m/p*-Ph); 128.3 (*m/p*-Ph); 127.6 (*m/p*-Ph); 126.9 (*m/p*-Ph); 126.7 (*m/p*-Ph); 119.7 (10,15-C). UV–vis (CH<sub>2</sub>Cl<sub>2</sub>, λ<sub>max</sub> [nm] (log ε)): 332 (4.29), 444 (4.85), 457 (4.86), 636 (4.28), 669 (4.36). HRMS (ESI, *m/z*): 688.1757 (688.1726 for C<sub>46</sub>H<sub>30</sub>N<sub>3</sub>Zn<sup>+</sup>).</sub></sub>

**Chlorozinc(II) 11,16-Bis(4-nitrophenyl)-6,6,21,21-tetraphenyl-*meta*-benzi-6,21-porphodimethene (7–ZnCl).** <sup>1</sup>H NMR (CDCl<sub>3</sub>, 298 K): 8.26 (4H, m, 11,16-*m*); 7.65, 7.58 (4H, 2 × b, 11,16-*o*); 7.45, 7.34, 7.28 (ABC<sub>2</sub>: 3-H, 22-H, 2,4-H, <sup>3</sup>J<sub>AC</sub> = 8.1 Hz, <sup>4</sup>J<sub>BC</sub> ≈ 1.8 Hz); 7.31–6.25 (10H, m, 6,21-*o,m,p*-Ph); 7.17, 7.07, 6.75 (AB<sub>2</sub>C<sub>2</sub>, 6,21-*p*-Ph', 6,21-*m*-Ph', 6,21-*o*-Ph', <sup>3</sup>J<sub>AB} ≈ <sup>3</sup>J<sub>BC} ≈ 7.5 Hz); 6.51, 6.22 (AB: 9,18-H, 8,19-H <sup>3</sup>J<sub>AB} = 4.8 Hz); 6.16 (2H, s, 13,14-H). <sup>13</sup>C NMR (CDCl<sub>3</sub>, 298 K): 178.0 (7,20-C); 148.8 (12,15-C); 148.0 (11,16-*p*); 146.1 (10,17-C); 145.0 (1,5-C); 144.9 (11,16-*i*); 144.8 (6,21-*i*-Ph'); 142.4 (6,21-*i*-Ph); 141.3 (11,16-C); 136.3 (8,19/9,18-C); 132.0 (3-C); 131.8, 131.5 (11,16-*o*); 131.1 (6,21-*o*-Ph); 129.7 (6,21-*o*-Ph'); 129.3 (2,4-C); 128.4 (6,21-*m*-Ph'); 128.3 (8,19/9,18-C); 128.2 (6,21-*m*-Ph); 128.1 (22-C); 127.6 (6,21-*p*-Ph); 127.4 (13,14-C); 126.6 (6,21-*p*-Ph'); 122.8 (11,16-*m*); 63.5 (6,21-C).</sub></sub></sub>

**Cadmium(II) Insertion (General Procedure for 5–CdCl and 7–CdCl).** A benzporphyrin (**1** or **3**, 2–20 mg) and anhydrous CdCl<sub>2</sub> (molar excess) are refluxed in CHCl<sub>3</sub>/MeCN (10 mL + 10 mL, up to 2 h, depending on the ligand). The reaction can be monitored by means of UV–vis spectroscopy. The reaction mixture is then filtered and evaporated to dryness, yielding quantitatively the pure Cd complex.

**Chlorocadmium(II) 6,11,16,21-Tetraphenyl-*m*-benzporphyrin (5–CdCl).** <sup>1</sup>H NMR (CDCl<sub>3</sub>, 298 K): 7.53–7.40 (m, 6,11,16,21-Ph); 7.71, 7.26, 5.46 (AB<sub>2</sub>C: 3-H, 2,4-H, 22-H, <sup>4</sup>J<sub>AC</sub> = 1.7 Hz, <sup>3</sup>J<sub>AB} = 7.8 Hz); 7.49, 6.79 (AB: 8,19-H, 9,18-H, <sup>3</sup>J = 5.0 Hz), 7.02 (s, 13,14-H). <sup>13</sup>C NMR (CDCl<sub>3</sub>, 298 K): 170.8 (10,17-C); 163.1 (12,15-C); 153.5 (7,20-C); 141.8 (*i*-Ph/6,21-C); 140.0 (*i*-Ph/6,21-C); 139.6 (1,5-C); 139.5 (*i*-Ph/6,21-C); 135.6 (8,19-C); 134.8 (13,14-C); 133.9 (3-C); 133.4 (9,18-C); 133.4 (6,21/11,16-*o*-Ph); 132.6 (6,21/11,16-*o*-Ph); 131.8 (2,4-</sub>

C); 129.1 (6,21/11,16-*m*-Ph); 127.8 (6,21/11,16-*m*-Ph); 127.8 (6,21/11,16-*p*-Ph); 127.5 (6,21/11,16-*p*-Ph); 117.4 (11,16-C); 82.8 (22-C).

**Chlorocadmium(II) 11,16-Bis(4-nitrophenyl)-6,6,21,21-tetraphenyl-*meta*-benzi-6,21-porphodimethene (7–CdCl).** <sup>1</sup>H NMR (CDCl<sub>3</sub>, 298 K): 8.27, 8.25 (4H, 2 × ~d, 11,16-*m*); 7.68, 7.55 (4H, 2 × ~d, 11,16-*o*); 7.54, 7.40, 7.23 (AB<sub>2</sub>C: 3-H, 2,4-H, 22-H, <sup>3</sup>J<sub>AB} = 8.1 Hz, <sup>4</sup>J<sub>BC} = 2.0 Hz); 7.33–7.26 (6H, m, 6,21-*m,p*-Ph); 7.19–7.14 (6H, m, 6,21-*o*-Ph, 6,21-*p*-Ph'); 7.06 (4H, ~t, 6,21-*m*-Ph'); 6.71 (4H, ~d, 6,21-*o*-Ph'); 6.47, 6.12 (AB: 9,18-H, 8,19-H, <sup>3</sup>J<sub>AB} = 4.7 Hz, <sup>4</sup>J<sub>CdH} = 3.2 Hz, 4.6 Hz), 6.18 (2H, s, 13,14-H, <sup>4</sup>J<sub>CdH} = 4.4 Hz). <sup>13</sup>C NMR (CDCl<sub>3</sub>, 298 K): 176.5 (7,20-C); 150.3 (12,15-C); 148.0 (11,16-*p*); 145.9 (10,17-C); 145.5 (11,16-*i*); 145.1 (1,5-C); 143.7 (6,21-*i*-Ph'); 142.4 (11,16-C); 142.1 (6,21-*i*-Ph); 136.4 (9,18-C); 132.7 (3-C); 131.8, 131.6 (11,16-*o*); 130.9 (6,21-*o*-Ph); 130.6 (2,4-C); 129.8 (6,21-*o*-Ph'); 128.3 (8,19-C); 128.3 (6,21-*m*-Ph'); 128.3 (13,14-C); 128.3 (6,21-*m*-Ph); 127.7 (6,21-*p*-Ph); 126.8 (6,21-*p*-Ph'); 126.5 (22-C); 122.8, 122.5 (11,16-*m*); 63.6 (6,21-C).</sub></sub></sub></sub></sub>

**6,11,16,21-Tetraphenyl-*m*-benzporphyrin, Mercury Complexes (5–HgCl, 5–HgOAc, 5–HgOCCF<sub>3</sub>).** These complexes are generated in situ by shaking a chloroform solution of **1** with an appropriate Hg(II) salt (HgCl<sub>2</sub>, Hg(OAc)<sub>2</sub>, Hg(OCCF<sub>3</sub>)<sub>2</sub>) or by titrating with a MeCN solution of the same Hg(II) salt. Progress of the reaction can be monitored by means of NMR or UV–vis spectroscopy. Complexes 5–HgX have limited stability and tend to hydrolyze. <sup>1</sup>H NMR (5–HgCl, CDCl<sub>3</sub>, 298 K): 7.51–7.40 (m, 6,11,16,21-Ph); 7.62, 7.17, 5.80 (AB<sub>2</sub>C: 3-H, 2,4-H, 22-H, <sup>3</sup>J<sub>AB} = 7.7 Hz, <sup>4</sup>J<sub>BC} = 1.7 Hz); 7.44, 6.70 (AB: 8,19-H, 9,18-H, <sup>3</sup>J = 4.9 Hz), 7.06 (s, 13,14-H). <sup>13</sup>C NMR (5–HgCl, CDCl<sub>3</sub>, 298 K): 171.4 (10,17-C); 163.1 (12,15-C); 153.6 (7,20-C); 142.1 (6,21/11,16-*i*-Ph); 141.0 (6,21-C); 139.9 (6,21/11,16-*i*-Ph); 138.3 (1,5-C); 136.2 (8,19-C); 134.5 (13,14-C); 133.5 (6,21/11,16-*o*-Ph); 133.0 (3-C); 132.5 (9,18-C); 132.5 (6,21/11,16-*o*-Ph); 132.3 (2,4-C); 129.0 (6,21/11,16-*m*-Ph); 127.9 (6,21/11,16-*m*-Ph); 127.6 (6,21/11,16-*p*-Ph); 127.5 (6,21/11,16-*i*-Ph); 117.5 (11,16-C); 89.2 (22-C). UV–vis (5–HgOAc, CH<sub>2</sub>Cl<sub>2</sub>, λ<sub>max</sub> [nm] (log ε)): 321 (4.46); 433 (4.74); 868 (4.21). MS (ESI, *m/z*): 824.0 (824.2 for C<sub>46</sub>H<sub>30</sub>N<sub>3</sub><sup>200</sup>Hg<sup>+</sup>).</sub></sub>

**Nickel(II) 6,11,16,21-Tetraphenyl-*m*-benzporphyrin (8–Ni).** Benzporphyrin (**1**, 15 mg) and NiCl<sub>2</sub> (5 mg, 1.6 equiv) are added to dry MeCN (20 mL) and refluxed for 4 h (reaction time can be shortened by adding a small amount of anhydrous K<sub>2</sub>CO<sub>3</sub>). The mixture is evaporated, yielding a solid residue, which is redissolved in a small volume of CH<sub>2</sub>Cl<sub>2</sub> and evaporated again (this step is repeated up to three times to remove traces of MeCN). The product is finally dissolved in CH<sub>2</sub>Cl<sub>2</sub> and filtered through a Teflon disk. One crystallization (CH<sub>2</sub>Cl<sub>2</sub>/MeOH) affords analytically pure 8–Ni. Yield: 10 mg (60%). <sup>1</sup>H NMR (CDCl<sub>3</sub>, 298 K): 7.81, 7.10 (A<sub>2</sub>B: 2,4-H, 3-H, <sup>3</sup>J<sub>AB} = 7.6 Hz); 7.55–7.38 (m, 24H, 6,11,16,21-Ph); 7.31 (s, 2H, 13,14-H); 7.14, 6.87 (AB: 8,19-H, 9,18-H, <sup>3</sup>J<sub>AB} = 5.2 Hz). <sup>13</sup>C NMR (CDCl<sub>3</sub>, 298 K): 159.2 (10,17-C); 151.6 (12,15-C); 149.1 (22-C); 146.7 (7,20-C); 142.8 (2,4-C); 140.8 (6,21-*i*-Ph); 138.8 (11,16-*i*-Ph); 137.7 (1,5-C); 135.8 (8,19-C); 133.6 (13,14-C); 132.2, 132.1 (6,21/11,16-*o*-Ph); 129.9 (9,18-C); 127.6 (× 2, 6,21-*m*-Ph, 11,16-*m*-Ph); 126.6 (× 2, 6,21-*o*-Ph, 11,16-*o*-Ph); 124.9 (3-C); 117.2 (11,16-C). UV–vis (CH<sub>2</sub>Cl<sub>2</sub>, λ<sub>max</sub> [nm] (log ε)): 364 (4.48), 435 (4.57), 695 (3.68), 816 (3.61), 912 (3.53). HRMS (ESI, *m/z*): 682.1809 (682.1788 for C<sub>46</sub>H<sub>29</sub>N<sub>3</sub><sup>58</sup>Ni + H<sup>+</sup>).</sub></sub>

**Chloronickel(II) 22-H-6,11,16,21-tetraphenyl-*m*-benzporphyrin (5–NiCl)** is obtained quantitatively by flushing a CHCl<sub>3</sub> solution of the diamagnetic 8–Ni with gaseous HCl. UV–vis (CH<sub>2</sub>Cl<sub>2</sub>, λ<sub>max</sub> [nm] (log ε)): 316 (4.48), 429 (4.70), 806 (4.17).

**Chloronickel(II) 5,10,15,20-Tetraphenyl-*p*-benzporphyrin (6–NiCl).** *p*-Benzporphyrin (**2**, 5 mg) and NiCl<sub>2</sub> (5 mg) are refluxed in a CHCl<sub>3</sub>/MeCN mixture for 6 h (progress of the reaction can be monitored with UV–vis spectroscopy). The solution is evaporated, and the remaining MeCN was removed by adding small portions of CH<sub>2</sub>Cl<sub>2</sub> to the residue and evaporating to dryness. The resulting solid is dissolved in a small volume of CH<sub>2</sub>Cl<sub>2</sub>, filtered, and evaporated again. The product

does not require further purification; it can, however, be crystallized from hexane. HRMS (ESI,  $m/z$ ): 682.1817 (682.1788 for  $C_{46}H_{30}N_3^{58}Ni^+$ ).

**Chloronickel(II) 11,16-bis(4-nitrophenyl)-6,6,21,21-tetraphenyl-meta-benzi-6,21-porphodimethene (7-NiCl)** is obtained analogously. HRMS (ESI,  $m/z$ ): 926.2302 (923.2272 for  $C_{58}H_{38}N_5O_4^{58}Ni^+$ ).

**NMR Spectroscopy.** NMR spectra were recorded on a Bruker Avance 500 spectrometer (base frequencies:  $^1H$  500.13 MHz,  $^{13}C$  125.77 MHz,  $^{113}Cd$  106.05 MHz,  $^{199}Hg$  89.16 MHz) equipped with a broadband inverse gradient probehead, a dual  $^1H$ – $^{13}C$  gradient probehead, or a direct broadband probehead. Spectra were referenced to the residual solvent signals. Except for NOESY, all 2D experiments were gradient-selected. In the case of heteronuclear correlation spectra, the acquisition resolution in the  $t_1$  domain was between 1k and 2k which enabled precise determination of chemical shifts and, in some cases, observation of satellite patterns (Figure S7, Supporting Information). Assignments of diamagnetic  $^1H$  spectra were obtained from COSY/TOCSY and NOESY/ROESY maps, and assignments of  $^{13}C$  spectra were made on the basis of  $^1H$ – $^{13}C$  HSQC and HMBC experiments. 1D variants of gradient-selected HMQC and HSQC sequences were employed to record the  $^{113}Cd$ - and  $^{199}Hg$ -filtered spectra, with evolution times optimized for the observed range of coupling constants.

Paramagnetically shifted spectra were recorded with fast recycle times (usually below 100 ms). The maximum spectral width allowed by the hardware was ca. 200 ppm for  $^1H$ , so that the extreme low-field signals were recorded in separate runs.

Longitudinal relaxation times ( $T_1$ 's) were determined using the standard inversion recovery technique. The recovery time was varied from 1  $\mu s$  to 1 s in an approximately logarithmic fashion, so as to cover the broad range of decays.

**X-ray Data Collection and Refinement.** Crystal data and refinement details are given in Table S1 (Supporting Information). The data were collected on a Kuma KM4CCD  $\kappa$ -axis diffractometer with graphite-monochromated Mo  $K\alpha$  radiation and processed using the accompanying software. The structures were solved by heavy atom or direct methods (SHELXS97<sup>84</sup>) and refined by the full-matrix least-squares method on all  $F^2$  data using the SHELXL97 program.<sup>85</sup>  $\psi$ -scan absorption correction was applied.<sup>86</sup> Hydrogen atoms were refined as riding with the following exceptions. In the structure of **5**–NiCl, positional parameters of H(22) were refined independently of C(22). For structures **5**–CdCl and **6**–NiCl, the inner hydrogens (H(22) and H(21), H(22), respectively) were refined with a distance restraint of 0.95(1) Å (DFIX instruction).<sup>85</sup> In all structures, isotropic thermal parameters of all H's were scaled as  $1.2 \cdot U_{eq}$  of the respective *ipso*-C.

**DFT Calculations and AIM Analysis.** DFT calculations for structures **5'**–CdCl and **6'**–CdCl were performed with the Gaussian 98 program.<sup>87</sup> Geometry optimizations were carried out within unconstrained  $C_1$  symmetry, with starting coordinates derived from X-ray structural data. Becke's three-parameter exchange functional<sup>88</sup> with the

gradient-corrected correlation formula of Lee, Yang, and Parr (DFT-(B3LYP))<sup>89</sup> were used with the LANL2DZ basis set.<sup>90</sup> Harmonic vibrational frequencies were calculated using analytical second derivatives. Both structures were found to have converged to a minimum on the potential energy surface.

Topology of the electron density,  $\rho$ , was analyzed using the PROAIM package.<sup>91</sup> Critical points (defined by vanishing gradient of electron density,  $\nabla\rho = 0$ ) found in this analysis are characterized by the corresponding value of  $\rho$  and its curvature. The curvature of electron density at a point is described by the three ordered eigenvalues of the Hessian (matrix of second derivatives):  $\lambda_1 < \lambda_2 < \lambda_3$ . A negative value of  $\lambda$  signifies a maximum of  $\rho$  along the direction of the eigenvector. Depending on the number of negative eigenvalues, a critical point is denoted (3,–3) (three negative eigenvalues), (3,–1) (two), (3,1) (one), and (3,3) (all positive eigenvalues).<sup>75</sup>

The (3,–3) points are normally located at the positions of nuclei. The (3,–1) points are associated with chemical bonds and are therefore termed bond critical points (BCPs). The two gradient lines emanating from a BCP and ending at the (3,–3) points of the bonded atoms form an atomic interaction line (called a bond path in a system at equilibrium). In a cyclic system, the ring center is occupied by a (3,1) point (ring critical point), and in a cage system a (3,3) point is found inside a cage. Importantly, the multiplicities  $N$  of the different types of critical point satisfy the Poincaré–Hopf relationship

$$N_{(3,-3)} - N_{(3,-1)} + N_{(3,1)} - N_{(3,3)} = 1 \quad (3)$$

Additional parameters used to describe a critical point are the Laplacian,  $\nabla^2\rho = \lambda_1 + \lambda_2 + \lambda_3$ , and ellipticity,  $\epsilon = (\lambda_1/\lambda_2) - 1$ . The Laplacian is also expressed as

$$\frac{\hbar^2}{4m} \nabla^2\rho = 2G + V \quad (4)$$

where  $V$  and  $G$  stand for the potential and kinetic energy density, respectively. Their sum

$$H = G + V \quad (5)$$

is the total energy density at the given point.<sup>82</sup>

AIM bond orders were evaluated according to the method of Mayer et al.<sup>80</sup> In this particular methodology, the overlap integrals of orbitals are calculated over proper atomic domains defined by AIM. Therefore, the results are expected to be less basis-set-dependent and less ambiguous as compared to the classical Mulliken-type schemes of bonding analysis.<sup>75</sup> The Mayer method was shown to emphasize the ionic nature of the bonds.<sup>80</sup>

**Acknowledgment.** This work was supported by the State Committee for Scientific Research of Poland (KBN) under Grant 4 T09A 147 22 (L.L.-G., M.S., and L.S.). M.S. thanks the Foundation for Polish Science for financial support. DFT calculations were performed at the Supercomputer Centers in Wrocław and Poznań.

**Supporting Information Available:** X-ray data (CIF file and tables), NMR and UV–vis spectra, AIM details (PDF). This material is available free of charge via the Internet at <http://pubs.acs.org>.

JA039384U

(88) Becke, A. D. *Phys. Rev. A* **1988**, *38*, 3098.

(89) Lee, C.; Yang, W.; Parr, R. G. *Phys. Rev. B* **1988**, *37*, 785.

(90) Hay, P. J.; Wadt, W. R. *J. Chem. Phys.* **1985**, *82*, 270, 284, 299.

(91) Biegler-Koenig, F. W.; Bader, R. F. W.; Tang, T. H. *J. Comput. Chem.* **1982**, *3*, 317.

(84) Sheldrick, G. M. *SHELXS97 – Program for Crystal Structure Solution*; University of Göttingen, 1997.

(85) Sheldrick, G. M. *SHELXL97 – Program for Crystal Structure Refinement*; University of Göttingen, 1997.

(86) *XPREP Data Preparation and Reciprocal Space Exploration Program*; Bruker Analytical X-ray Systems, 1997.

(87) Frisch, M. J.; Trucks, G. W.; Schlegel, H. B.; Scuseria, G. E.; Robb, M. A.; Cheeseman, J. R.; Zakrzewski, V. G.; Montgomery, J. A.; Stratmann, R. E.; Burant, J. C.; Dapprich, S.; Millam, J. M.; Daniels, A. D.; Kudin, K. N.; Strain, M. C.; Farkas, O.; Tomasi, J.; Barone, V.; Cossi, M.; Cammi, R.; Mennucci, B.; Pomelli, C.; Adamo, C.; Clifford, S.; Ochterski, J.; Petersson, G. A.; Ayala, P. Y.; Cui, Q.; Morokuma, K.; Malick, D. K.; Rabuck, A. D.; Raghavachari, K.; Foresman, J. B.; Cioslowski, J.; Ortiz, J. V.; Stefanov, B. B.; Liu, G.; Liashenko, A.; Piskorz, P.; Komaromi, I.; Gomperts, R.; Martin, R. L.; Fox, D. J.; Keith, T.; Al-Laham, M. A.; Peng, C. Y.; Nanayakkara, A.; Gonzalez, C.; Challacombe, M.; Gill, P. M. W.; Johnson, B. G.; Chen, W.; Wong, M. W.; Andres, J. L.; Head-Gordon, M.; Replogle, E. S.; Pople, J. A. *Gaussian 98*; Gaussian, Inc.: Pittsburgh, PA, 1998.